Structural Dynamics of the Vimentin Coiled-Coil Contact Regions involved in Filament Assembly as revealed by Hydrogen-Deuterium Exchange

Aiswarya Premchandar[†], Norbert Mücke[&], Jarosław Poznański[†], Tatjana Wedig[&], Magdalena Kaus-Drobek[†], Harald Herrmann[§, *], Michał Dadlez [†, $, *]

[†] Institute of Biochemistry and Biophysics, Polish Academy of Sciences, Pawińskiego 5A, 02-106 Warsaw, Poland

[$] Warsaw University, Biology Department, Institute of Genetics and Biotechnology, Miecznikowa 3, Warsaw, Poland

[&] Biophysics of Macromolecules, German Cancer Research Center (DKFZ), Im Neuenheimer Feld 280, D-69120 Heidelberg, Germany

[§] Division of Molecular Genetics, German Cancer Research Center (DKFZ), Im Neuenheimer Feld 280, D-69120 Heidelberg, Germany, and Institute of Neuropathology, University Hospital Erlangen, D-91054 Erlangen, Germany

Running title: *Structural dynamics in vimentin assembly*

*To whom the correspondence should be addressed: 1) Prof. Dr. hab. Michał Dadlez, Institute of Biochemistry and Biophysics, Department of Biophysics, 02-106 Warsaw, Tel.: +48 22 5923 471; Fax: +48 22 658 4766; michald@ibb.waw.pl; 2) Prof. Dr. Harald Herrmann, Institute of Neuropathology, University Hospital Erlangen, D-91054 Erlangen, Germany, Tel.: +49 (0)9131 85-34782, Fax: +49 (0)9131 85-26033, harald.herrmann@uk-erlangen.de

1

ABSTRACT

Intermediate filaments (IF) are major constituents of the cytoskeleton of metazoan cells. They not only are responsible for the mechanical properties but also for various physiological activities in different cells and tissues. The building blocks of IFs are extended coiled-coil–forming proteins exhibiting a characteristic central α-helical domain ("rod"). The fundamental principles of the filament assembly mechanism and the network formation have been widely elucidated for the cytoplasmic IF protein vimentin. Also, a comprehensive structural model for the tetrameric complex of vimentin has been obtained by X-ray crystallography in combination with various biochemical and biophysical techniques. To extend these static data and investigate the dynamic properties of the full-length proteins in solution during the various assembly steps, we analyzed the patterns of hydrogen-deuterium exchange (HDex) in vimentin and in four variants carrying point mutations in the IF consensus motifs present at either end of the α-helical rod that cause an assembly arrest at the unit-length filament (ULF) stage. The results yielded unique insights into the structural properties of subdomains within full-length vimentin, in particular in regions of contact in α-helical and linker segments that stabilize different oligomeric forms such as tetramers, ULFs, and mature filaments. Moreover, HDex analysis of the point-mutated variants directly demonstrated the active role of the IF-consensus motifs in the oligomerization mechanism of tetramers during ULF formation. Ultimately, using molecular dynamics simulation procedures, we provide a structural model for the subdomain-mediated tetramer–tetramer interaction via "cross-coiling" as the first step of the assembly process.

INTRODUCTION

Intermediate filament (IF) proteins form highly resilient filaments that are markedly resistant to mechanical stress. Mediated by prominent cytolinker proteins of the plakin family and motor proteins, they integrate actin filaments and microtubules to establish a functional cytoskeleton in metazoan cells and promote optimal tissue function (1). Apart from their basic mechanical function in maintaining cell flexibility, they are also involved in multiple cellular activities that range from cell division and motility to the topological organization of transmembrane channels (2, 3). Owing to these multi-functional properties of IF proteins, mutations in IF-encoding genes cause almost 100 different human inherited diseases (4, 5). One of the most studied IF proteins, vimentin, forms IFs typical for mesenchymal cells, including endothelial cells, lymphocytes, and the eye lens epithelium (6). Of note, vimentin has long been implicated in many aspects of cancer initiation and progression, including tumorigenesis, epithelial–mesenchymal transition, and the metastatic spread of cancer (7), making this protein an attractive potential target for cancer diagnosis and therapy (8). Therefore, to develop mechanistic insight into the behavior of IF proteins in their normal and pathogenic forms, it is crucial to work out their detailed three-dimensional structures at different stages of oligomerization and filament assembly.

IF proteins form extended coiled-coils that associate into macromolecular assemblies under a broad range of ionic conditions. For this reason, crystallization of the entire protein as well as that of higher order complexes was not possible up to now. Nevertheless, IF protein structure generation using X-ray crystallography has been successfully achieved for various fragments by a "divide and conquer" approach (9, 10). In these crystals, the fragments were in a monomeric, dimeric, or even tetrameric association state. With complementary techniques such as chemical cross-linking (11) and site-directed spin labeling coupled with electron paramagnetic resonance (SDSL-EPR) (12), a structural model for the dimeric as well as the tetrameric vimentin complex was eventually obtained at atomic resolution, excluding the intrinsically disordered N- and C-terminal regions (13, 14). In the present "crystallographic" view, the structural organization of a vimentin monomer comprises a central, mostly α-helical "rod" domain flanked by intrinsically disordered non–α-helical N-terminal ("head") and C-terminal ("tail") domains. The rod consists of two equally sized α-helical subdomains termed coil 1 (146 amino acids) and coil 2 (140 amino acids), which are connected by the 16 amino acid–long non–α-helical linker segment L12 (Figure 1A). Coil 1 is divided into a short coil 1A and a longer coil 1B segment. Linker L1 connecting the coil 1A and B subdomains is 8 amino acids long and evolutionarily highly conserved; similar to other intrinsically disordered domains, it may optionally form a distinct structure

(15). Indeed, in the crystal of a larger fragment derived from coil 1, linker L1 adopts an α-helical fold without being involved in the coiled-coil formation of coil 1A and coil 1B (13). Coil 2 represents a continuous α-helix in which the first 35 amino acids form hendecad repeats establishing a right-handed helix with a very large pitch. Hence, in the dimer, the two chains essentially form parallel helices, which are designated as "paired bundle" or pb (16). We refer to this region as coil 2A throughout the text and want to stress that it contains former coil 2A, linker L2, and 11 amino acids of former coil 2B. We find this distinction important because this segment is structurally and functionally different from the rest of coil 2.

The remaining segment of coil 2, here referred to as coil 2B, is in heptad configuration, allowing coiled-coil formation, including a "stutter" at position 350 that represents a brief interruption in the heptad pattern by a single hendecad repeat (16). A unique feature of vimentin and sequence-related IF proteins such as desmin and neurofilament proteins is represented by a short segment preceding coil 1A, the pre-coil domain (*pcd*), which exclusively contains amino acids that are compatible with α-helix formation although no structure has been determined to date (orange box in Figure 1A; see also (17)). A corresponding structural motif is absent from other IF proteins such as keratins and nuclear lamins.

The first step in vimentin assembly is the formation of in-parallel and in-register coiled-coil dimers; two of these dimers associate into an antiparallel, approximately half-staggered tetramer (Figure 1B). This tetrameric complex forms during renaturation of vimentin from 8 M urea to low-salt buffers and constitutes the smallest soluble complex that can be handled in non-denaturing conditions (18). The addition of salt initiates filament assembly, probably by releasing the strongly basically charged head domain from an unproductive interaction with the acidic rod; the increase in ionic strength subsequently results in the lateral association of an average of eight tetramers into a one-unit-length filament referred to as ULF (19, 20). Filaments form by longitudinal annealing of ULFs to short filaments and of ULFs and short filaments with each other (1). During filament elongation, an approximately 3-nm overlap is formed between the various dimers of two filaments *via* the interaction of the end segments of

coil 2 and coil 1A, as determined by chemical crosslinking and electron microscopy (21). This intermolecular "coupling," the principal physical interaction for filament elongation, constitutes the "head-to-tail" overlap. Eventually, filaments can grow into very long structures to more than 20 µM in length (22). These filaments are very stable *in vitro* because they exchange sub-units at a very low rate (23).

During this dynamic process of filament assembly, many different domains interact in concert in a complex and hierarchical fashion. We now need to define the molecular interactions that lead to this observed formation of higher oligomers, like octamers, ULFs, and filaments. Such information is of course not easily obtained from X-ray–based studies of protein fragments because truncations may eliminate crucial contacts in the complete molecules and thus result in non-native contacts in the crystal (24). Also, proteins that naturally organize into oligomeric complexes are extremely sensitive to even small alterations. Small incremental effects of the aberrant subunit interactions accumulate with the number of subunits. This may lead to significant shifts in the equilibrium between different oligomeric forms. Therefore, results obtained for fragments cannot be directly extrapolated to fit into the context of fully native molecules. Studies on full-length, unmodified proteins in solution in native conditions are therefore necessary for selecting, verifying, and integrating the fragmented information obtained to date. For this purpose, monitoring the exchange kinetics of peptide amide hydrogen atoms by hydrogen-deuterium exchange (HDex) in native proteins can be highly informative, and this method is indeed well suited for studying the formation of coiled-coil proteins. Following HDex reactions, mass spectrometry (MS) can precisely assess the retarded exchange for different protein forms in their native conditions across unlimited molecular mass ranges. This rationale has motivated other authors to study different coiled-coil proteins like fibrinogen (25) or troponin C (26) in their fully native context. In particular, we have also demonstrated previously in the keratin pair K8 and K18 that the coiled-coil regions exhibit variable levels of protection from exchange, indicative of the hierarchical networks of hydrogen bonds stabilizing α-helices (27). The differences in the protection level between different oligomeric forms

may indicate the interactions in distinct domains established during the formation of filaments from oligomers. Motivated by the above considerations, we have undertaken an extensive HDex study of vimentin tetramers, ULFs, and filaments. Unlike keratins, vimentins form homopolymers, and the assembly process can be arrested at the ULF stage by introducing point mutations at either end of the α-helical rod (28). Last but not least, because the structures of all of the coiled-coil segments in vimentin are known at atomic resolution, the direct correlation between the molecular structure and the HDex dynamics of vimentin in combination with molecular dynamics simulation studies yielded unique insights into the principal contact sites that establish and stabilize the octamer and eventually the filament.

RESULTS

During the first seconds after salt addition step, ULFs very rapidly form followed by a less dynamic longitudinal annealing reaction of ULFs with each other and of ULFs with short filaments (19, 29). In this way, uniform and flexible IFs that are several microns in length are formed over time (30). The elongation reaction involves an approximately 3-nm overlap of the start of coil 1A with the end of coil 2, the two segments representing the so-called IF-consensus motifs, conserved in all classes of IF proteins (24, 31). Interestingly, this very dynamic reaction can be completely stopped by a single amino acid change in this domain of coil 1A, i.e., mutating a highly conserved and bulky tyrosine to leucine at position 117 of human vimentin, Y117L (28). Also, the corresponding mutation of tyrosine to a leucine on the other end of the α-helical rod in coil 2B, i.e., at position 400 (Y400L), produces the same effect: complete stop of assembly at the ULF state (data not shown). The reasoning underlying mutation of tyrosine to leucine in both cases was that we expected it would tremendously stabilize the coiled coil at these positions and furthermore would impede the opening of the coiled coils as observed by X-ray crystallography for the vimentin Y117L mutant (28, 31). Moreover, we were curious if the replacement of these two tyrosines by a small and non-hydrophobic amino acid such as serine would have a different effect. However, by electron microscopy, we demonstrated that both vimentin Y117S and vimentin Y400S did not assemble

beyond the ULF state either. Three of the mutants, Y117L, Y400S, and Y400L, formed regularly shaped ULFs of about 60 nm length and a diameter of 12 nm as observed for wild-type vimentin too (19, 32). In contrast, the ULFs formed by vimentin Y117S are missing the characteristic and uniform "cigar-like" shape of the other three mutant proteins but adopts a more roundish structure (Figure 1E). Therefore, we conclude that the three mutants forming regularly shaped ULFs represent a reliable ULF-state structure, though "frozen" in longitudinal assembly. Moreover, the soluble Y117S subunits form ULFs that do not reach the exactly laterally aligned organization seen with wild-type vimentin and the three other mutants and may therefore constitute a polymorphic association.

Analytical Ultracentrifugation of Soluble Vimentin Complexes—Cytoplasmic IF proteins are notoriously insoluble under physiological ionic conditions. However, we have previously demonstrated by analytical ultracentrifugation that two IF proteins, vimentin and desmin, form stable and homogenous tetrameric complexes with an *s*-value of around 5 S under various low ionic strength conditions, such as 5 mM Tris-HCl (pH 8.4), and at the protein concentrations usually employed in assembly experiments, i.e., 0.1 to 0.5 mg/ml (19, 33, 34). This tetrameric state is usually not altered by single amino acid changes; however, in the case of desmin disease variants, we recently revealed that 2 out of the 14 desmin mutations investigated caused a significant shift of the mutant protein complexes to a higher *s*-value, i.e., 9.5 S and 11.9 S (35). Nevertheless, these two mutant desmins formed relatively regular filaments though with lower number of molecules per filament cross-section. To investigate the impact of the vimentin mutations on their complex state, we analyzed the four ULF-stop mutant variants by analytical ultracentrifugation at low ionic strength. Three of them, Y117S, Y400L, and Y400S, sedimented like wild-type vimentin (Figure 1C), whereas Y117L exhibited a shift in sedimentation velocity centrifugation experiments to higher *s*-values (Figure 1C-a; blue trace). Thus, we conducted sedimentation equilibrium runs to determine the mass of the complexes in a concentration-dependent manner (33). Here, Y117L sedimented with a mass equivalent to ~380 kDa corresponding to an octameric complex. Only at low protein concentration, Y117L sedimented as a tetramer,

4

with a mass extrapolated to ~220 kDa (Figure 1C-c).

Next, we assembled the four ULF variants under standard assembly conditions and subjected them to sedimentation velocity runs. They exhibited very uniform distributions, peaking at ~45 S, except for Y117S, which sedimented with an *s*-value of ~60 S possibly reflecting its more compact form (Figure 1D; red trace). We also investigated by analytical ultracentrifugation the properties of mutant ULFs when they were assembled at high concentration and then diluted tenfold, analogous to the procedure applied in HDex analysis, when the sample to be analyzed is diluted tenfold with D_2O. Of note, the assembly at high concentration had only minor effects on the sedimentation properties of ULFs as judged by their behavior in velocity sedimentation runs (Figure 1D, filled symbols). Hence, Y117S shifted to slightly higher *s*-values, whereas Y400L sedimented at slightly lower *s*-values. In summary, all four mutant proteins stayed in a soluble form with the very notable absence of aggregates. This favorable behavior was not influenced by assembly occurring at higher protein concentration, i.e., 2 mg/ml. Together with their regular appearance in electron microscopy, these data confirm that the mutant ULFs form defined nano-particles that reproduce a transition state in the assembly of wild-type vimentin.

HDex Patterns in Vimentin Oligomers—To compare the dynamic nature of coiled coils in tetramers and filaments, we measured HDex patterns both in NaPi buffer (Figure 2A, tetramers) and NaPi buffer with 100 mM KCl (Figure 2B, filaments). We chose two incubation times for analysis: 10 s to provide information on less stable regions and 20 min for reporting on more protected regions. By and large, a significant fraction of proton amides was fully exchanged in the head domain, the tail domain, and the linker L12 region, even at the shortest incubation time in both tetramers and filaments. In all other regions, an intermediate fraction of exchange was observed − in less protected regions after 10 s and more strongly protected parts after 20 min. Exchange across almost the entire length of coil 2B is represented by a single, long peptide because this region was not susceptible to pepsin proteolysis for undetermined reasons (Figure 3). However, signals from this long peptide were retrieved from the raw data and manually appended to the dataset.

In an otherwise unprotected head domain in wtVim_Tet, the C-terminal part of the head domain that corresponds to the *pcd* showed weak protection (Figure 2A). A similar weak protection continued into the N-terminal segment of coil 1A and terminated abruptly at position 117. This region also encompasses the sequence LNDR_114, a motif that is conserved across all IF proteins. In stark contrast, the residues between positions 118−133 in the C-terminal region of coil 1A were well protected, with exchange detectable only at the longer incubation times. This experiment indicates the partition of coil 1A in tetramers into two regions differing distinctly in their susceptibility to exchange. In the linker L1 region, an increased exchange marked an apparent discontinuity within coil 1 while we observed strong protection for nearly the entire coil 1B. The regions close to the N-terminus and the C-terminus of coil 1B barely began to register some exchange after 20 min of incubation. These two regions are the most stable segments of the vimentin tetramer. Protection levels sharply decreased at linker L12. Interestingly, the coil 2A, i.e., the paired bundle region (*pb*), also registered a similar lack of protection. These segments are significantly more dynamic than the C-terminal segments of coil 1A and coil 1B. The N-terminal peptide of coil 2B at positions 300−310 also showed only weak levels of protection. Within coil 2B, the region 380−395 close to the C-terminus was well protected, seemingly providing a structural anchor, whereas the C-terminal peptide itself became fully exchanged after 20 min. These results indicate a strict pattern of well-protected regions intertwined with the flexible ones. Higher dynamics was not restricted to the linker regions but included regions expected to form coiled-coils such as the N-terminal segments of both coil 1A and coil 2A.

The Crucial Contact Regions in Vimentin Filaments—The general pattern of protected and unprotected regions in tetramers was greatly retained upon transition into filaments, with several regions showing the same levels of protection in tetramers and filaments, as in the C-terminal segment of coil 1A and coil 1B (Figure 2B). The regions that were already stabilized in the tetramers did not reveal further stabilization in the filaments. However, there were also pronounced differences

in the filaments, which are best illustrated in the differential plot (Figure 2C; schematically represented in 2D). This plot represents the difference in the fraction of exchanged protons observed between the two oligomeric states, either after 10 s of incubation (black bar) or after 20 min (red bar). The N-terminal segment of coil 1A gained substantial protection during the transition from tetramers to filaments. The difference remained equally strong after 20 min of incubation, which reflected upon the significant stabilization of H-bonding networks in this region. In other words, the N-terminal region of coil 1A formed a stable α-helix in filaments but not in tetramers. This stabilization was accompanied by loss of residual protection of the *pcd* segment in filaments. Thus, the partition between head and coil 1A regions became much stricter in filaments than in tetramers. In contrast, the C-terminal segment of coil 1A retained a relatively stable α-helix in filaments.

Two other regions that became stabilized in the transition to filaments were coil 2A and the C-terminal peptide 400–408 of coil 2B. The entire coil 2A segment in filaments was no longer fully susceptible to exchange as was the case for tetramers. The stabilization was not very strong, however, because main-chain hydrogens in this region were completely exchanged after 20 min. In contrast, in filaments, the C-terminal coil 2B peptide retained some protection even after 20 min. This effect was accompanied by slight exposure for exchange of another coil 2B peptide at position 388−393. The three regions stabilized in filaments—the N-terminal segments of coil 1A, coil 2A as well as the C-terminal segment of coil 2B—were the only segments of the tetramers that became more structured during incorporation into filaments. Therefore, we propose that these regions represent the contact sites that hold the filaments together.

Discerning the Contact Sites within the Vimentin ULFs from Those in Filaments—To further dissect the networks of interactions and narrow down their roles at different stages of filament formation, we also measured HDex patterns in four mutants that are arrested at the ULF state after initiation of assembly. This assembly block is permanent, i.e., no filaments form even after 24 h of incubation. Two sites among the contact regions, one at position 117 within the N-terminal segment of coil 1A and another at position

400 in the C-terminal segment of coil 2B, were chosen for mutation studies. These included highly conserved tyrosines within highly conserved sequence motifs, also referred to as "IF-consensus motifs." Among the mutants that were selected for this study, the Y117L mutant protein formed octamers at low ionic strength (Figure 1C) and ULFs of ~40 S at the higher ionic strength. This comparison was ideal to distinguish interactions that are important in the formation of ULFs from those important in filament formation. The patterns of deuterium uptake in the Y117L mutant in its octameric state ($Y117L_{Oct}$) and its ULF state ($Y117L_{ULF}$) are represented in Figures 4A and 4B, respectively. The transition from octamers to ULFs in the mutant was accompanied by stabilization of two regions: the N-terminal segment of coil 1A and coil 2A (Figure 4C, D). Most notably, the transition into ULFs was not accompanied by protection in the C-terminal region of coil 2B, which is an important event in the formation of vimentin IFs.

When compared to vimentin tetramers ($wtVim_{Tet}$), the exchange patterns in the Y117L octamer ($Y117L_{Oct}$) were mostly similar but with some significant differences (Figure 5A). In the *pcd* region, the residual protection observed in $wtVim_{Tet}$ was lost in $Y117L_{Oct}$, while the N-terminal segments of coil 1A, as well as of coil 2A, were more protected in the $Y117L_{Oct}$ than in $wtVim_{Tet}$. Also, we observed stabilization in peptide 388−393 in the C-terminal region of coil 2B of the $Y117L_{Oct}$ (Figure 5A), indicating a structural cross-talk between the C-terminus of coil 2B and the mutation site 270 amino acids upstream in the molecule, already at the stage of laterally associated tetramers. When the HDex uptake in $wtVim_{Tet}$ and $Y117L_{ULF}$ was compared (Figure 5B), the stabilization in coil 2A was stronger than in 1A, contrary to that observed for wtVim on the transition of tetramers to filaments (Figure 2C). Thus, the Y117L mutation led to increased stability at the low ionic strength in two regions out of three stabilized in $wtVim_{Fil}$. Such stabilization was thus impeding the transition of ULFs to elongated filaments because the mutant was arrested at the ULF state. Despite the stabilization of the N-terminal segment of coil 1A in $Y117L_{ULF}$, the degree of stabilization was weaker when compared to that of $wtVim_{Fil}$ (Figure 5C; compare also Figure 2D and 4D). This loss of stability in the N-terminus of coil 1A and a lack of stabilization of coil 2B between amino acids 400–

408 in the mutant ULFs indicates that the stability gain observed between these N-terminal and the C-terminal motifs is a consequence of filament formation and therefore seen only in wtVim$_{Fil}$.

Another major finding is that coil 2A was more stable in Y117L$_{ULF}$ than in wtVim$_{Fil}$ (Figure 5C). Leu117, which is in the *d* position of the heptad, introduces an overly stable interaction between the two helices of coil 1A (28). This difference in the α-helical organization of coil 1A affected the stability of coil 2A in both octamers and ULFs of the mutant protein. The coil 2A, being more dynamic in nature, registered these changes only at shorter incubation periods. These comparisons clearly identified the regions of contact in the lateral association of tetramers to ULFs and the longitudinal annealing of ULFs to filaments. Comparison of the deuterium exchange patterns obtained for wtVim$_{Tet}$ and Y117L$_{ULF}$ indicated that ULFs were stabilized by contacts between the N-terminal domains of coil 1A and coil 2A. Comparing the corresponding data for Y117L$_{ULF}$ with those of wtVim$_{Fil}$ revealed further stabilization in the N-terminal segment of coil 1A and that of the C-terminal coil 2B peptide in filaments (Figure 5C). This stabilization indicated that these two regions are filament-forming contact sites and include the highly conserved helix termination region Y$_{400}$RKLLEGEE$_{408}$. Also, coil 2A revealed higher protection in Y117L$_{ULF}$ than in wtVim$_{Fil}$, indicating aberrantly stable Leu117–coil 2A interactions absent in wtVim that may have caused the arrest of filament formation in the mutant (Figure 5C). Interestingly, the transition to filaments in wtVim also led to the relative exposure of the 388−393 region of coil 2B, an effect absent in the mutant ULFs (compare Figure 2D and 4D). Contrary to wtVim, the whole region 380–399 became evenly protected in both assembly forms of the mutant i.e. octamer and ULFs.

The Coil 1A Mutation Y117S Disrupts the Formation of Higher Order Oligomers—Unlike the bulky tyrosine residue or the very hydrophobic leucine residue, the serine residue, which is occasionally found in *a* or *d* position in coiled coils, does not have a significant impact on the coiled-coil geometry (28). Substitution of Tyr117 with serine had drastic effects on vimentin assembly at the ULF level. In low-salt conditions, the Y117S mutant formed tetramers; however, under assembly conditions, it assembled into open, round ULF-like

structures as revealed by electron microscopy of a negatively stained specimen (Figure 1E). Comparison of wtVim$_{Tet}$ and Y117S$_{Tet}$ (Figure 5D) revealed decreased stability in the *pcd* head region and coil 1A of the mutant. The mutation appeared to have deranged the entire coil 1A structure and that of the preceding *pcd* region in the tetrameric form of the Y117S mutant. The perturbation of the *pcd* and the coil 1A region also affected the arrangement of coil 2A in the second dimer of the tetrameric unit. When these tetramers laterally assembled upon increase of ionic strength, the destabilization of these regions apparently led to a less compact association with the coil 2A of the neighboring tetramers. Of note, in the Y117S mutant, the association of tetramers to ULF-like complexes did not cause any difference in the exchange patterns because they remained almost unaltered between Y117S$_{Tet}$ and Y117S$_{ULF}$ (data not shown). This similarity in exchange patterns could be gauged based on comparisons between the wtVim$_{Tet}$ and Y117S$_{Tet}$ (Figure 5D), as well as between wtVim$_{Tet}$ and Y117S$_{ULF}$ (Figure 5E): the same regions were affected to a similar degree in either case. Missing stabilization in coil 1A, especially around the N-terminus, and coil 2A in the Y117S$_{ULF}$ was also evident in comparisons with wtVim$_{Fil}$ (Figure 5F). Weak stabilization of coil 2A and lack of stabilization in coils 1A and coil 2B upon shifting to assembly conditions indicated that the ULF-like assembly happened *via* non-specific side-chain interactions without any evident stabilization of the coiled coils. Unlike in Y117L$_{ULF}$, even the C-terminal segment of coil 1A was not stable in the Y117S$_{ULF}$. A common feature that the Y117S$_{ULF}$ shares with that of Y117L$_{ULF}$ is stabilization around the 388–393 segment (Figure 5C and 5F).

In summary, filament formation of non-mutated vimentin leads to a shift in protection from the near-C-terminal end to the very end of coil 2B (see Figure 2C, D). It has to be noted, though, that the stabilization of segment 388–393 in both point mutants was already present at the stage of tetramers (Figure 5A and 5D), in which, according to a classic scheme of ULF assembly (1), the region of mutation and the stabilized region are not in direct contact. Nevertheless, the observed structural coupling of these two regions could be achieved by the involvement of head and/or tail regions.

7

Isotopic Envelopes of Peptide 108-QELNDRFANY-117: the Effects of Replacing Y by L or S—We extracted the isotopic envelopes of peptides $Q_{108}-X_{117}$ from wtVim as well as mutants Y117L and Y117S at higher ionic strengths, where they are expected to exist in filaments, ULFs, and ULF-like structures respectively (Figure 6). wtVim$_{Fil}$ showed practically no deuterium exchange and remained unperturbed even at higher incubation times. In comparison, Y117L$_{ULF}$ registered weak levels of exchange, indicating reasonable protection at the shorter incubation time. However, this protection was lost at longer incubation times. The serine mutant Y117S, which cannot form regularly organized ULFs, exhibited unrestricted susceptibility to exchange for this peptide. Substitution of Y117 with either L or S led to the near-complete or complete disruption of the filament assembly. Thus, Y117 at the N-terminus of coil 1A plays a pivotal role in the filament elongation process. In the assembly process, the N-terminal segment of coil 1A began as being entirely flexible in tetramers (wtVim$_{Tet}$, Y117S$_{Tet}$), gained considerable stability in octamers (Y117L$_{Oct}$) and ULFs (Y117L$_{ULF}$), and eventually underwent further stabilization in filaments (wtVim$_{Fil}$).

Effects of Mutating Tyrosine at Position 400 in the IF Consensus Motif of Coil 2B—Leucine substituting tyrosine at position 400 in the highly conserved region YRKLLEGEE segment blocked the assembly at the ULF stage as well. Consistent with the results obtained for Y117L (Figure 4C), the Y400L$_{ULF}$ registered increased levels of protection in coil 2A and a minor change in the N-terminal region of coil 1A (Figure 7A). Interestingly, the non-cleavable region in the coil 2B of the mutant protein became longer by 10 amino acids (Figure 3C). The mutation of the bulky tyrosine residue to leucine most probably restored the normal coiled-coil distance in this region of coil 2B, as seen in the crystal for coil 1A in the corresponding Y117L mutation, thereby propagating closure of the coiled coil to the end of coil 2. As a consequence, the originally used cleavage site in the wtVim was not accessible to pepsin in the Y400L mutant protein.

Interestingly, when compared with wtVim$_{Tet}$, Y400L$_{Tet}$ revealed increased coil 1A C-terminal stability and a lack of protection of the *pcd* region (Figure 7B). A similar loss of *pcd* protection was observed for both Y117X mutants (Y117L:

Figure 5A; Y117S: Figure 5D). However, in the Y400L mutant, the mutation site is separated from the *pcd*–coil 1A segment by about 280 amino acids, which nevertheless was affected by this mutation in the tetrameric state. Thus, the interactions in which the *pcd* segments were engaged in wtVim$_{Tet}$ seemed to involve the C-terminal segments of coil 2B because an extended, longer coil 2B rod in the mutant tetramer destabilized them. Such far-reaching interactions may be mediated by the involvement of head/tail regions.

The molecular properties of the Y400L$_{ULF}$ differ from those of the Y117L$_{ULF}$ by lower stabilities observed for coil 1A and coil 2A (Figure 7C), which is expected because these regions are overly stable in Y117L. The results thus indicate that the inability of the Y400L mutant to form filaments originates from the change in the α-helical arrangement at the end of coil 2B, leading to an elongated coil 2B rod and the inability of this region to properly engage in the interactions with coil 1A. Also, a recurrent lack of structure formation of the *pcd* segment at the stage of tetramers was observed commonly in the Y117X and Y400L mutants, but the role of the *pcd* structure, present in wtVim at the tetramer state, is not clear.

The corresponding tyrosine to serine mutation, Y400S, generated a mutant protein that formed more regular ULFs compared to the Y117S protein, as monitored by electron microscopy (data not shown). In Y400S, coil 1A and coil 2A became more stable in the transition to ULFs. Coil 1A stabilization was weak, and the C-terminal segment of coil 2B, bearing the mutation site, remained unchanged (Figure 7D), as expected for mutants arrested at the ULF stage. Observed changes were similar to those seen for Y117L$_{ULF}$ (Figure 4C) and Y400L$_{ULF}$ (Figure 7A). Comparison of Y400S$_{Tet}$ with wtVim$_{Tet}$ (Figure 7E) again showed the structural coupling between the N- and C-terminal regions in tetramers, with loss of *pcd* structural organization and increased stability of the central region of coil 1A in Y400S, accompanied by increased stability of a short region in coil 2A. However, an increased stability of the 388–393 region, observed for Y117S$_{Tet}$ (Figure 5D) and Y117S$_{ULF}$ (Figure 5E), was not present in Y400S$_{Tet}$ (Figure 7E) and Y400S$_{ULF}$ (Figure 7F). The precise status of this region could not be gauged in Y400L$_{ULF}$ because the undigested fragment was

longer and spanned from residues 299 to 418. The data presented in Figure 7F show that the Y400S$_{ULF}$ was more stable and well-structured than in Y117S mutant, albeit with a marked flexibility in the 388–393 region. The structural coupling of the N- and C-terminal segments of the rod, responsible for deprotection of the 388–393 region in wtVim$_{Fil}$ (Figure 2D), but not in both Y117X mutant proteins (Figure 5), was retained in Y400S despite the fact that the Y400S mutation site is only 7 amino acids downstream from segment 388–393.

CD Spectra of Vimentin Peptides—To verify if the observed coil 1A–coil 2A–coil 2B interactions can also be seen in vimentin fragments, we synthesized three peptides: (1) 1A, covering the head-coil 1A interface (residues 102–138); (2) 2A, covering the coil 2A–coil 2B interface (residues 264–298); and (3) 2B, covering the coil 2B–tail interface (residues 383–412). These peptides are entirely soluble in assembly buffer over a wide concentration range. We analyzed the circular dichroism (CD) spectra of these peptides, alone and in different combinations. In addition, we measured the concentration dependence of these spectra. For the 1A peptide, a characteristic signal, corresponding to the α-helical structure was obtained (Figure 8, black line). At a starting concentration of 100 µM, mean residue ellipticity $[\theta]_{MRW}$ at 222 nm was ca. 17,000 deg*cm^2*dmol^{-1}, indicating an α-helical content >50%. Thus, in the isolated peptide, the highly dynamic α-helical region spanned a larger fraction of the sequence, most likely covering both its N- and C-terminal parts, contrary to HDex results in the context of tetramers in which the N-terminal segment 108–117 showed no protection and thus no stable α-helical structure. With decreasing concentration, the signal became much weaker, reaching 5000 deg*cm^2*dmol^{-1} at 8.8 µM (Figure 8A). This behavior indicated that the peptide spontaneously forms dimers at least, and CD allowed tracing of monomer–dimer equilibrium changes upon subsequent dilution. These results are in agreement those of a previous study of the coil 1A peptide (28).

When an equimolar mixture of the 1A and 2A peptides was analyzed, the measured molar ellipticity at 222 nm was higher than the sum of molar ellipticities measured for the separated peptides (Figure 8B, compare dark blue solid line with dark blue dash-dot line), indicating a non-

additive effect and implying interactions between 1A and 2A peptides. Similar non-additivity was observed when the 2B peptide was added to the mixture of 1A and 2A peptides (compare the red solid line with the red dash-dot line in panel B). In the presence of 2B peptide, the measured molar ellipticity became larger than the arithmetic sum of 1A and 2A and 2B ellipticities. The ternary complex formed spontaneously and became more stable because the concentration dependence of the ternary complex became significantly sharper (Figure 8C), with the mean residue ellipticity of the ternary complex being lowest at high concentrations and highest at low concentrations. In conclusion, these experiments showed that the three selected regions of vimentin tend to interact spontaneously even for isolated peptides. It is plausible, thus, that the role of the flanking head region is to prevent their premature interactions by destabilizing the α-helix in the N-terminal coil 1A in lower order oligomers.

Investigation of Coil 1A and Coil 2A Segment Cross-coiling by Molecular Dynamics Simulations—Based on X-ray crystallographic data, cross-coiling of coils 1A of neighboring tetramers has been suggested as a potential basis for lateral stabilization of tetramers in ULFs (13) and defined there as a new structural fold, occurring between two coiled-coil dimers from two different tetrameric complexes oriented in an anti-parallel way and resulting in a type of four-stranded coiled coil. According to the HDex data provided in this study, both the coil 1A and the coil 2A α-helical segment are stabilized in ULFs. Therefore, we suggest that coil 2A participates in the cross-coiling mechanism. Moreover, we observed that in the Y117L mutant, the stabilization of the coil 2A α-helix was much stronger than in non-mutated vimentin and that this stabilization most probably blocked further longitudinal association of ULFs. Leucine at position 117 was found previously to cause strong stabilization of the coiled-coil structure in coil 1A homodimers (28), so it is plausible that the observed enhanced stabilization of coil 2A in the Y117L mutant originates from direct interactions between coils 1A and 2A, in an as yet unknown manner. Fine-tuned reorganization of the antiparallel coiled-coil segments of coil 1A and 2A α-helices is thus a likely cross-coiling mechanism providing ULF stabilization. This inference, along with the observation by Nicolet et

al. (36) of the propensity of coil 2A fragments to form non-native homo-tetramers (3KLT structure), led us to hypothesize that the coil 1A–coil 2A cross-coiling complex forms a similarly organized hetero-tetramer in which one of the coil 2A dimers is substituted by a pair of coil 1A α-helices (Figure 9A, upper panel). The X-ray structure of the coil 1A–L1–coil 1B segment was obtained previously for the coil 1A Y117L mutant (1ABL structure from (13)). In this structure, the coil 1A segment was also found to homo-tetramerize (Figure 2D of (13)), with the coil 1B segment forming a dimer, from which coil 1A segments splay apart, as illustrated in the dimer structure deposited as 3S4R (Figure 9A, lower left panel). The overlay of the two coil 1A α-helices from the 3S4R dimer on two of the four helices of the 3KLT homotetramer is shown in Figure 9A, lower right panel. The optimum overlay shown was obtained by testing each possible mutual register of $a-d$ heptad position residues in coils 1A and hendecad a-d-h positions in coils 2A (marked yellow in 3KLT and orange in 3S4R, respectively) along the tetramer axis, without modification of any parameters of the X-ray–derived structures. The overlay still allowed burying of a substantial number of hydrophobic residues in the hetero-tetramer. Because of partial overlap of the coil 1B region between 3S4R and 3UF1 structures, the cross-coiled heterotetramer from panel A could then be overlaid with the X-ray structure of the coil 1B tetramer 3UF1 (Figure 9B). To do this overlay, the chains from 3S4R and 3UF1 were concatenated at the best overlap of Cα atom coordinates of residues Leu$_{149}$ to Leu$_{189}$, belonging to the coil 1B α-helices, present in 3S4R and 3UF1. The whole structure of the coil 1A–coil 1B tetramer, cross-coiled with the coil 2A dimer, was subjected to a series of rationally restrained molecular dynamics procedures, leading to the optimized structure (Supplementary Movie S1, Supplementary Movie S2).

DISCUSSION

To obtain more insight into the subdomain dynamics of the coiled-coil protein vimentin, we have mapped in-solution HDex patterns for the authentic full-length protein in its different accessible oligomeric states. These experiments ensured unique insight into their structural properties in fully native structural context. We have provided direct experimental identification of the regions responsible for stabilization of three principal oligomeric forms, i.e., tetramers, ULFs, and mature filaments. We have found that when wtVim tetramers combine to form filaments, three regions become stabilized: the N-terminal segment of coil 1A, coil 2A, and the C-terminus of coil 2B. With the Y117L vimentin mutant, we could also separate specific contact sites responsible for the lateral association of tetramers to ULFs versus the longitudinal elongation of ULFs into filaments. We could thus identify the N-terminal half of coil 1A as participating both in the lateral association of tetramers into ULFs (when paired with coil 2A) and in longitudinal elongation (when paired with the coil 2B C-terminus). Moreover, in replacing bulky aromatic residues located in d positions of the heptad repeat patterns, we have correlated the effects of a series of mutations in positions 117 (N-terminal part of coil 1A) and 400 (C-terminal end of coil 2B) with their HDex patterns. These results enabled us to further our understanding of the molecular mechanisms mediating filament assembly.

HDex Provides New Insights into Coiled-coil Domain Dynamics—Our study decisively extends previous data obtained with methods such as X-ray crystallography or SDSL-EPR because experiments were directly performed on unmodified, full-length vimentin in solution. X-ray crystallization provided detailed static snapshots of vimentin fragments deprived of the native structural context, in which large sections of the molecule were missing in the crystals. Studying X-ray structures of fragments precludes capturing far-range native interactions that might stabilize higher order contacts during oligomerization. Moreover, in the absence of such authentic native contacts, non-native networks entangling the molecule in the crystal lattice and possibly distorting the proper structural preferences may have taken over. Also, the static nature of X-ray structures masks protein dynamics and provides a restricted description of the coiled-coil status in IF proteins in which α-helices are either present or absent. In contrast to this description, our study indicates a high level of variability of helix dynamics. In contact regions, distinct levels of dynamics are the differentiating feature characteristic for each step of tetramer–ULF–filament assembly. This focus rationalizes

their description rather in terms of ensembles of α-helical elements of variable stability, with all scenarios possible, from rapidly unfolding-folding and highly dynamic elements to extremely stable sections that are not susceptible to proteolytic cleavage even in denaturing conditions. Therefore, the application of HDex has revealed new insights centering on the dynamics of functional subdomains within the α-helical rods of the coiled-coil dimers in successive states of the assembly process.

The most stable regions found at coil 1B termini, named "structural anchors" revealed strongly retarded exchange. This behavior is illustrated in Fig. 4 A, B by the results obtained after 20 minutes of exchange (red marks), which clearly show that these regions barely start to exchange their amide protons to deuterium. Rates of exchange correlate strictly with the frequencies of H-bond breaking events, which are decisive for helix stability. In stable helices, main chain H-bonds break less frequently than in unstable helices. Stability of helices is usually strongly coupled to the existence of inter-helical contacts (side chain-side chain interactions), isolated stable helices in peptides are rare. Thus, if any new inter-helical interactions (even involving solely side chains) appear, they are expected to increase the stability of the participating helices and the effect can be measured by HDex. If helices in these regions were additionally stabilized in filaments, we would have observed further retardation of exchange, which is not the case. In these regions differences in exchange levels between filaments and tetramers were minor if any. Moreover, our results show that the rod 1B center retains in filaments a similar level of increased exchange, as compared to coil 1B termini (i.e. "structural anchors"). Therefore, we observed no stabilization also in the relatively less protected rod 1B center. That is why we focused our attention on the three regions (coil 1A N-terminus, coil 2A, and coil 2B C-terminus) that revealed a clear and very strong stabilization. Rod 1B is known to stabilize dimeric structures, so this region might be crucial for early stages of oligomerization but not necessarily at the later steps.

HDex Investigation of Keratin Assembly—HDex patterns were determined previously for another set of IF proteins, i.e., keratin K8/K18 (27). In spite of different assembly conditions (10 mM Tris-HCl, pH 7.5, for keratins as compared to 2 mM NaPi, 100 mM KCl, pH 7.5, for vimentin), the general pattern of exchange when compared after 10 s of exchange (compare Figure 2A of this manuscript with Figure 3A, 3B in (27)) is principally the same with a lack of protection in the head, linker L12, and tail regions and uniform high protection of coil 1B juxtaposed with uneven protection of the N-terminus of coil 2. However, there are also significant differences: 1) In vimentin filaments, coil 1A is equally stable in both the N- and C-terminal parts, whereas in keratins, the N-terminal part of coil 1A is still less protected than that of the C-terminal part. 2) Coil 2 in vimentin is partitioned into a partially protected coil 2A and a more strongly protected remaining portion, whereas for keratins, the well-protected region covers only a short peptide in the center of coil 2. In keratins, coil 2A is more strongly protected than both flanking regions: linker L12 and the N-terminal segment of coil 2B. In contrast, in vimentin, coil 2A is distinctly less protected than the remainder of coil 2B. Two of the regions gaining protection in the transition from tetramers to filaments are the same in keratins and vimentin, namely the coil 1A N-terminal and the coil 2B C-terminal segment. The third region of protection that covers coil 2A in vimentin is shifted in keratins towards the center of coil 2. Due to inefficient pepsin proteolysis of coil 2B of vimentin, the behavior of the corresponding region could not be assessed.

Distinct Hydrogen Exchange Dynamics within Coil 1—The above-mentioned difficulties in the integration of the results obtained by crystallography for truncated versions of vimentin can be exemplified by the results of the X-ray analysis of the coil 1A region 102−138, which in one structure (1GK7) is a monomeric α-helix (10), whereas in the other (3SSU) (13), it is completely disordered. We have found that the N-terminal part of this region, at positions 108−117, including the strictly conserved $LNDR_{114}$ motif (37), becomes converted to a stable α-helix upon transition from tetramers to ULFs and filaments, being thus engaged in both stages of filament formation. In agreement, the coil 1A segment of vimentin has been indicated before as critical for both the lateral (A_{11}) and the longitudinal (A_{CN}) association (38), as concluded from chemical cross-linking studies (39, 40). Also, in an SDSL-EPR study of vimentin that

scanned positions 1−108 (41), the region 104−108, directly preceding the 108−117 region, was one of the two affected and stabilized most strongly in the transition from ULFs to filaments.

In solution, the coil 1A segment itself (102−138) exists in a monomer–dimer equilibrium, whereas upon mutation of tyrosine 117 to leucine, this fragment forms a dimer (28). In agreement, the CD spectra of the 1A peptide presented here show strong concentration dependence, reflecting this equilibrium. In the crystal of this fragment (10), a monomeric α-helix was found, retaining only the curvature characteristic for a coiled coil because of crystal contacts. However, in the context of the longer fragment (99−189) (13), no electron density was observed for coil 1A or the L1 region, indicating their disordered status. For these reasons, it was hypothesized that the relative instability of the coil 1A dimer and the separation *via* the linker L1 from the stable coiled-coil dimer formed by the two coil 1B segments may enable a bi-modal switch between an open monomeric α-helical state and the coiled-coil state in this region (28). Obviously, this structural flexibility is important for longitudinal annealing of ULFs and for maturation of filaments when structural rearrangements are required to establish a stable end state of these macromolecular assemblies (13). Our results, obtained for authentic full-length vimentin, indicate that the dynamic status of coil 1A is restricted to a region ranging from amino acids 102 to 117, which switches between full exposure in tetramers and substantial stability in filaments. They indicate further that the C-terminal segment 118 to 138 of coil 1A retains stability similar to coil 1B at all stages of tetramer–filament transition. The linker L1 region has been found to be either unstructured in X-ray analysis (13) or coalescing into a α-helical rod conformation continuous with coils 1A and 1B and retaining a rigid stutter-like character as judged by SDSL-EPR spectroscopy (14). Our results indicate that L1 is distinct from the flanking α-helical segments of coil 1A and 1B segments in the context of full-length vimentin, as this region is clearly marked by increased susceptibility to exchange both in tetramers and filaments.

A longer N-terminal vimentin fragment, containing residues 1–138, i.e., the head region and coil 1A, has been shown to form dimers in solution (9). The head region is indispensable for tetramer, ULF, and filament formation because headless

vimentin forms only dimers under low ionic strength conditions and tetramers of the A_{22} type under assembly conditions (33). This pattern indicates the importance of head–rod electrostatic interactions involved in the salt-inducible transition to ULFs and filaments. Interestingly, our study showed an H-bonded structure in the last 20 C-terminal amino acids of the head segment, present in tetramers but absent in filaments. This very segment, termed the *pcd* region, was previously predicted to have the potential to form an α-helix (42), though only for SHC III (desmin/vimentin) and SHC IV (neurofilament proteins) but not for SHC I and II (keratins) and SHC V (lamins) IF proteins. Supported by head–rod interactions, helical *pcd* segments may pair with the C-terminal region of coil 1A in tetramers. In ULFs, the *pcd* segments may be replaced by inter-tetrameric coil 2A helices when high ionic strength destabilizes the head–rod complex. These interactions may be required at the tetramer stage, for instance, to provide protection against a premature A_{22}-type interaction. Hence, the head domains may play an indispensable role in preventing off-pathway interactions and guiding the tetramers into the productive oligomerization pathway. Further, the *pcd* region harbors two serines, S82 and S86, which are potential targets for the phosphorylation-dependent dynamics of vimentin filaments. Indeed, it has been shown that both serines are subject to the action of three different kinases during mitosis and that their phosphorylation mediates robust reorganization of the vimentin filament system in cells (43).

Distinct Hydrogen Exchange Dynamics within Coil 2—Comparison of HDex patterns in wtVim and the Y117L mutant protein, for which assembly is arrested at the ULF stage, allowed us to identify the coil 2A as a contact site for the N-terminal segment of coil 1A in ULF formation and to show that the coil 2A helix gains substantial stability in ULFs. This assumption is in agreement with the lateral assembly of A_{11}-type tetramers formed by the anti-parallel alignment of two parallel coiled coils of rod 1 segments, originally identified based on chemical cross-linking studies (11). In this arrangement of tetramers, these two regions are juxtaposed (see Figure 1 and Figure 8B in (42)).

For the coil 2A region, a hendecad repeat parallel α-helix bundle was proposed (44). The X-

ray analysis of the amino acid segment 261−335 (D3) fragment (36) revealed a parallel α-helical bundle for the two coil 2A chains at positions 263−302, followed by a regular left-handed coiled coil for the two 2B segments. This arrangement was, however, stabilized by a non-native homo-tetrameric structure in the crystal, with the 263−302 regions overlapping to form a complex of two antiparallel-oriented dimers (3KLT in PDB). In solution, coil 2 forms dimers under physiological salt conditions (33). Similar to coil 1A, the coil 2A α-helix seems to be marginally stable, and this dynamic behavior is masked in X-ray experiments by non-native interactions. On the other hand, in assembled filaments, SDSL-EPR experiments indicated a highly ordered structure for the segment representing residues 281–304 (L2 region) of vimentin (45). Collected SDSL-EPR and X-ray data consistently indicate an α-helical structure of L2 and the coalescence of the entire rod 2 into a single α-helix, partly forming a coiled coil, partly an α-helical bundle. However, the intrinsic structural preferences of this region, similar to coil 1A, seem to be weak. Our result shows that an α-helical structure in the region consisting of coil 2A and the N-terminus of coil 2B is absent in tetramers while it becomes significantly stabilized in ULFs and filaments.

Lateral Association of Tetramers to Octamers by Cross-coiling—For assembly of vimentin tetramers into filaments, the ionic strength is raised by addition of a concentrated salt solution. Thereby, the very basic first 77 amino acids of the head domain of each monomer, comprising 11 arginines and no acidic residue, are relieved from intra-tetrameric interactions engaging acidic clusters situated on the rod domains of the neighboring dimers (29). A segment in the center of each head domain, associated with the opposite coil 2A segment is thus set free for new interactions that would pull two tetramers together. As an immediate consequence, the two tetramers may engage in inter-tetrameric interactions *via* the contacting sites, such that one coiled-coil dimer segment of one tetramer engages in the interactions with the coiled-coil dimer in the neighboring tetramer. In this process, two heterotetrameric complexes of the dimeric coil 2A–linker L12 segments from one of the interacting tetramers, with the dimeric coil 1A segments of the second tetramer may serve as a driving force for this interaction (Figure 10). The

new anti-parallel interaction of coil 1A and 2A segments from two tetramers may be referred to as "cross-coiling", according to the orientation found in crystals and illustrated by the molecular dynamics simulations experiments (Figure 9, Supplementary Movie S1, Supplementary Movie S2). Thus, for the lateral association of tetramers into octamers to occur, the coil 1A and coil 2A segments, originating from different tetramers, pair in a cross-coiled structure. One of the two available coil 1A segments in each tetramer is engaged in the complex with one of the two available coil 2A segments, stabilizing an octamer. The remaining, free coil 1A and 2A regions can further cross-coil in an inter-octameric way (not shown), enabling oligomer growth into 16-mers, 32-mers, and finally to ULFs, after circularization of a 32-mer by the interaction between flanking tetramers. Of note, such a cross-coiling scheme allows tetramers to be linked into higher order oligomers *via* a flexible linker L12, being 15 amino acids long. Connecting tetramers by flexible linkers enables maintenance of the structural flexibility of the assembly of coiled-coil rods even within higher order oligomers and a relative loose packing of tetramers in ULFs, previously indicated by SAXS data (46).

The topology of the new cross-coiling complex requires that the C-terminus of one of the L12 linkers passes in between two L1 linker segments, as illustrated in the inset of Figure 10 (also see the molecular model in Supplementary Movie S3). Interestingly, the regions of the L12 and L1 linkers, which are in contact in the model, are highly conserved within class III and IV intermediate filament proteins (Table 1). The C-terminus of L12 in type III and IV SHC proteins contains a D-X-X-K-P-D/E motif, while the C-terminus of L1 contains a highly conserved basic residue (marked blue in Figure 10 inset), accompanied by a strong cluster of negatively charged residues at the coil 1B N-terminus (marked red). Such an arrangement of charged residues provides additional stability for the proposed cross-coiling complex where the salt bridges E153–K262 (magenta arrow) and R145–D264 (red arrow) could be found. A conserved proline (marked green in Table 1), deprived of the side chain, fills the space between two L1 chains in the model. In NF-M and NF-H, proline is substituted by T or C, also residues of small volume. In SHC classes III and IV proteins, strict requirements seem thus to be

13

imposed on the transition region between the flexible L12 region and structured coil 2A and between L1 and coil 1B, which may be crucial for the effective molecular mechanism of cross-coiling.

Such pronounced rearrangements of dimeric chains yield octameric complexes with a geometry that most probably prepares the way for further octamer–octamer interactions. A further stepwise association to 16-mer and eventually 24- and 32-mer may proceed in a circular fashion, or in a topologically more complex association mode with an inner core arrangement of two octamers, as suggested previously on the basis of data obtained by small angle X-ray scattering of full-length vimentin in solution (47). In the latter model, the next two octamers are more laterally associated and would actually leave space for two additional octamers as found in polymorphic ULFs with five and six octamers (20). However, already in this earlier study, it was noted that the SAXS data would also be compatible with a structural rearrangement of octamers during ULF formation. Here, we hypothesize that such a rearrangement of dimers occurs indeed in the first step of assembly during octamer formation, thus driving the reaction into the direction of polymers.

Filament Growth: Bi-directional Annealing of ULFs—HDex analysis indicated that the C-terminal segment of coil 2B corresponding to the IF consensus motif $Y_{400}RKLLEGEE_{408}$ (31) becomes stabilized upon transition of tetramers to filaments in wtVim, but not in the Y117L mutant, which is arrested at the ULF stage. This finding points to the role of this fragment in the longitudinal assembly of ULFs to filaments, achieved through the interaction with the N-terminal part of coil 1A, as coil 1A undergoes stronger stabilization in wtVim than in Y117L vimentin (compare Figure 2C, D, and Figure 5A). In the X-ray structure of coil 2B segment Cys2 (328−411), a regular coiled-coil dimer extends up to position 405, where the two chains splay apart, and α-helix termination is attributed to the repulsion within the following acidic cluster EGEE (405–408) (10). Splaying was suggested to facilitate an interdigitating head-to-tail arrangement of coils 1A and the C-terminus of coil 2B into an overlapping parallel four-α-helix bundle in the transition from ULFs to filaments (37, 48). Of note, a similar acidic amino acid cluster, EAEE (286–289), in the *pb* domain of vimentin (former

L2 segment) readily incorporated into a α-helical structure (3KLT), indicating that charge density per se does not preclude α-helix formation. Here, the glutamic acids are in a *g*, *i*, and *j* positions of the hendecad repeat, whereas the glutamic acids in the end segment of the rod are in a *b*, *d*, and *e* positions. Hence, the glutamic acid in the *d* position may destabilize the α-helical structure significantly. In lamin tetramers, the dimers interact *via* their N- and C-terminal rod end segments (A_{CN} arrangement) (24) and a model assuming lateral overlap of corresponding helices and/or oppositely charged segments has been proposed (48). Overlapping of coil 1A and the C-terminal segment of coil 2B by 5 to 10 amino acids in mature filaments was suggested previously, based on cross-linking experiments, though in these experiments, the availability of lysine side chains for crosslinking may considerably shorten this distance because of the molecular length of the chemical crosslinker (11). The coil 2B C-terminal structure stabilization observed in this work may thus represent helix propagation over the splay point in filaments and incorporation of a more extended coil 2B C-terminal helix into the coil 1A–coil 2A network. In agreement, the CD analysis presented in our work demonstrated an intrinsic propensity of the C-terminal coil 2B region to form a ternary complex with the N-terminal coil 1A–coil 2A complex. Our data indicate that in the Y117L mutant, a strong interaction between coil 1A and the coil 2A region blocks the interaction with the C-terminal coil 2B segment. We, therefore, conclude that for the longitudinal annealing of ULFs with one another, the coil 1A–coil 2A complex of individual dimers needs to be rearranged to enable coil 1A–coil 2B interaction as the initial reaction of IF elongation.

EXPERIMENTAL PROCEDURES

Protein Chemical Methods and Electron Microscopy—The generation of point-mutated vimentin variants, purification of the recombinant proteins, and their assembly into tetramers and filaments were done as described before (33, 49). Electron microscopic (EM) analysis of vimentin assembly products was essentially done as described before (49). Both sedimentation velocity and sedimentation equilibrium centrifugation were performed with a Beckman model Optima XLA

instrument essentially as described for vimentin previously (33).

Sequencing and Peptide Analysis—The list of vimentin peptides was established using a non-deuterated sample. 5 µl of the protein stock solution (2−2.2 mg/ml) were diluted 10–fold by adding to 45 µl of 2 mM NaPi, pH 7.5 (H_2O reaction buffer). The sample was then acidified by mixing with 10 µl of H_2O stop buffer (2 M glycine buffer, pH 2.5). The sample was digested online using a 2.1 mm × 30 mm immobilized pepsin resin column (Porozyme, ABI, Foster City, CA) with 0.07% formic acid in water as the mobile phase (200 µl/min flow rate). The peptides were passed directly to the 2.1 mm × 5 mm C18 trapping column (ACQUITY BEH C18 VanGuard precolumn, 1.7 µm resin; Waters, Milford, MA). Trapped peptides were eluted onto a reversed phase column (Acquity UPLC BEH C18 column, 1.0 × 100 mm, 1.7 µm resin, Waters, Milford, MA) using an 8–40% gradient of acetonitrile in 0.1% formic acid at 40 µl/min, controlled by the nanoACQUITY Binary Solvent Manager. Total time of a single run was 13.5 min. All fluidics, valves, and columns were maintained at 0.5 °C using the HDX Manager (Waters, Milford, MA), except the pepsin digestion column, which was kept at 20 °C inside the temperature-controlled digestion column compartment of the HDX manager. The C18 column outlet was coupled directly to the ion source of SYNAPT G2 HDMS mass spectrometer (Waters, Milford, MA) working in Ion Mobility mode. Lock mass was activated and carried out using Leucine–enkephalin (Sigma). For protein identification, mass spectra were acquired in MS^E mode over the m/z range of 50–2000. The spectrometer parameters were as follows: ESI-positive mode, capillary voltage 3 kV, sampling cone voltage 35 V, extraction cone voltage 3 V, source temperature 80 °C, desolvation temperature 175 °C, and desolvation gas flow 800 L/h. The spectrometer was calibrated using standard calibrating solutions.

Peptides were identified using ProteinLynx Global Server software (PLGS, Waters, Milford, MA). We used a randomized database, with PLGS parameters set at minimum fragment ions per peptide = 4 and a false-positive rate threshold of 4%. The list of identified peptides, containing peptide m/z, charge, retention time, and ion mobility/drift time was passed to the DynamX 2.0

hydrogen-deuterium data analysis program (Waters, Milford, MA).

Hydrogen-deuterium Exchange Workflow—HDex experiments were carried out as described for the non-deuterated sample, with the reaction buffer prepared using D_2O (99.8% Cambridge Isotope Laboratories, Inc.) and pH (uncorrected meter reading) adjusted using DCl (Sigma). After mixing 5 µl protein stock with 45 µl D_2O reaction buffer, the exchange reactions were carried out at various times, as specified in the text, at room temperature. The exchange was quenched by reducing the pH to 2.5 by adding the reaction mixture to stop buffer (2 M glycine buffer, pH 2.5) and cooling on ice. Immediately after being quenched in the stop buffer, the sample was manually injected into the nanoACQUITY (Waters, Milford, MA) UPLC system. Subsequently, pepsin digestion, liquid chromatography (LC), and MS analyzes were carried out exactly as described above for non-deuterated samples.

Two control experiments were performed to account for in- and out-exchange artifacts, as described previously (50). In brief, to assess minimum exchange (in-exchange control), D_2O reaction buffer was added to stop buffer that had been cooled on ice before addition of protein stock, and this mixture was immediately subjected to pepsin digestion and LC/MS analysis as described above. The deuteration level in an in-exchange experiment was calculated and denoted as 0% exchange (M_{ex}^0). For out-exchange analysis, 5 µl of protein stock was mixed with 45 µl of D_2O reaction buffer, incubated for 24 h, mixed with stop buffer, and analyzed as described above. The deuteration level in an out-exchange experiment was calculated and denoted as 100% exchange (M_{ex}^{100}). The above experimental scheme enabled us to obtain the same set of fragments from the control and HDex experiments. Each experiment was repeated three times, and the results represent the mean of these replicates. *HDex Data Analysis*—The deuteration level for each peptide resulting from the exchange was calculated in an automated way using DynamX 2.0 software, based on the peptide list obtained from the PLGS program, further on filtered in the DynamX 2.0 program with the following acceptance criteria: minimum intensity threshold – 3000; minimum products per amino acids − 0.3. The analysis of the isotopic envelopes after the

exchange was carried out in DynamX 2.0 with the following parameters: RT deviation $\pm$ 15 s, m/z deviation $\pm$ 12.5 ppm, and drift time deviation $\pm$ 2-time bins. The average masses of peptides in the exchange experiment (M_{ex}) and the two control experiments (M_{ex}^0 and M_{ex}^{100}) obtained from the automated analysis were then verified by visual inspection. Ambiguous or overlapping isotopic envelopes were discarded from further analysis.

The percentage of relative deuterium uptake (% Deuteration) of a given peptide was calculated by taking into account both control values, following the formula:

$$\% \ Deuteration = \frac{(M_{ex} - M_{ex}^0)}{(M_{ex}^{100} - M_{ex}^0)} \times 100$$

Error bars for the difference in deuteration were calculated as standard deviations of three independent experiments. The value of the difference in exchange (ΔHDex) between two conditions of interest was obtained by subtracting the fraction of exchange measured in these conditions. Errors for ΔHDex value were calculated as the square root of the sum of variances of the subtracted numbers. Student's t-test for two independent samples with unequal variances and unequal sample sizes (also known as Welch's t-test) was carried out to evaluate differences in fraction exchanged between the same peptides in two different states. Final figures were plotted using OriginPro 8.0 (OriginLab) software.

Circular Dichroism Spectroscopy— Peptides of the following sequences— 1A:$_{102}$NEKVELQELNDRFANYIDKVRFLEQQN KILLAELEQL$_{138}$,

2A:$_{264}$DLTAALRDVRQQYESVAAKNLQEAEE WYKSKFADL$_{298}$,and

2B:$_{383}$YQDLLNVKMALDIEIATYRKLLEGEES RIS$_{412}$ —that covered the regions of interest in vimentin were obtained by chemical synthesis (1A, 2B were synthesized at PSL Peptide Specialty Laboratories GmbH, Germany, and the 2A peptide was ordered from GenScript). The peptide stocks were resuspended in 10 mM Tris-HCl, pH 8.4, and 100 mM NaF to a final concentration of 100 µM. The peptide complexes 1A–2A and 1A–2A–2B were prepared by mixing the respective peptides to a final concentration of 100 µM each, at room temperature an hour before CD measurements. CD

spectra of vimentin peptides and their complexes were recorded on the J−815 CD spectrometer (JASCO) over the spectral range 270−200 nm. Then, a series of 1.5-fold sample dilutions from the same stock was prepared, and CD spectra were again recorded. Altogether, samples at seven different concentrations were analyzed (100 µM, 66.7 µM, 44.4 µM, 29.7 µM, 19.8 µM, 13.2 µM, 8.8 µM). The molar ellipticity was calculated according to formula $[\theta] = \theta/(c \cdot l)$, and the mean residue ellipticity $[\theta]_{MRW}$ was calculated per peptide bond: $[\theta]_{MRW} = \theta/(c \cdot l \cdot n)$, where θ is the measured ellipticity in millidegrees, c is molar peptide concentration, l is the optical path length of the cuvette in millimeters, and n is the number of main-chain peptide bonds in all molecules in a given sample.

Molecular Modeling—All calculations were carried out using the Yasara Structure Package. Two alternative approaches were applied. In the first one, the preliminary structure of the heterodimer was obtained by the procedure of overlying accessible PDB structures of the tetrameric form of coil 2 domain ($_{264}$D-K$_{334}$; PDB: 3KLT) and coil 1A dimer ($_{102}$N-L$_{138}$; PDB: 3G1E), in which the possible shifts between coil 1A and coil 2A registers were scored according to a number of intermolecular Leu-Leu interactions, and the structural alignment with the highest scoring function was selected for further analyses (51). These included stepwise model extension by iterative structural alignment with 3S4R and 3UF1 structures, leading together to the model of larger part of heterodimer formed by $_{102}$N-I$_{249}$ and $_{265}$L-L$_{333}$ vimentin fragments.

In the alternative approach, the structure of the heterotetramer has been modeled by homology, using as templates 3SSU, 1QZW, 3S4R, and 3G1E PDB structures for coil 1A dimer and 3TRT, 1GK4, 3TNU, and 3KLT PDB structures for coil 2A, respectively. This approach enabled building the initial model of a larger part of the heterotetramer, which represented the crucial interaction between segments $_{81}$Q-Y$_{150}$ and $_{251}$E-N$_{350}$.

In the final step, both models were subjected to molecular dynamics simulations performed in the presence of explicit water molecules using standard Yasara2 forcefield with distance constraints introduced to preserve intrahelical backbone H-bonding pattern (3kcal/A). Additional distance constraints (8Å upper limit for

16

Cγ-Cγ distance) added for all intermolecular Leu-Leu interactions identified within 7Å limit were further iteratively updated in 100 ps intervals.

ABBREVIATIONS

IF, intermediate filaments; HDex-MS, hydrogen-deuterium exchange mass spectrometry; *pcd*, pre-coil domain; *pb*, paired bundle; EM, electron microscopy.

ACKNOWLEDGEMENTS

CONFLICT OF INTEREST

The authors declare that they have no conflicts of interest with the contents of this article.

AUTHOR CONTRIBUTIONS

AP, MD, and HH designed the study and wrote the paper. AP designed, performed, and analyzed all the HDex experiments. NM performed and analyzed the analytical ultracentrifugation experiments. JP helped with molecular docking and simulations for the vimentin ULF model. TW designed and constructed vectors for expression of recombinant wild-type vimentin and its mutant proteins and performed the EM experiments. MKD and AP performed and analyzed the CD data. All authors approved the final version of the manuscript.

REFERENCES

1. Herrmann, H., Strelkov, S. V, Burkhard, P., and Aebi, U. (2009) Intermediate filaments: primary determinants of cell architecture and plasticity. *J. Clin. Invest.* **119**, 1772–83

2. Vijayaraj, P., Kröger, C., Reuter, U., Windoffer, R., Leube, R. E., and Magin, T. M. (2009) Keratins regulate protein biosynthesis through localization of GLUT1 and -3 upstream of AMP kinase and Raptor. *J. Cell Biol.* **187**, 175–84

3. Colas, J., Faure, G., Saussereau, E., Trudel, S., Rabeh, W. M., Bitam, S., Guerrera, I. C., Fritsch, J., Sermet-Gaudelus, I., Davezac, N., Brouillard, F., Lukacs, G. L., Herrmann, H., Ollero, M., and Edelman, A. (2012) Disruption of cytokeratin-8 interaction with F508del-CFTR corrects its functional defect. *Hum. Mol. Genet.* **21**, 623–34

4. Szeverenyi, I., Cassidy, A. J., Chung, C. W., Lee, B. T. K., Common, J. E. A., Ogg, S. C., Chen, H., Sim, S. Y., Goh, W. L. P., Ng, K. W., Simpson, J. A., Chee, L. L., Eng, G. H., Li, B., Lunny, D. P., Chuon, D., Venkatesh, A., Khoo, K. H., McLean, W. H. I., Lim, Y. P., and Lane, E. B. (2008) The Human Intermediate Filament Database: comprehensive information on a gene family involved in many human diseases. *Hum. Mutat.* **29**, 351–60

5. Omary, M. (2004) Intermediate filament proteins and their associated diseases. *N. Engl. J. Med.* **351**, 2087–2100

6. Quinlan, R. A., Sandilands, A., Procter, J. E., Prescott, A. R., Hutcheson, A. M., Dahm, R., Gribbon, C., Wallace, P., and Carter, J. M. (1999) The eye lens cytoskeleton. *Eye (Lond).* **13**, 409–416

7. Kidd, M. E., Shumaker, D. K., and Ridge, K. M. (2013) The Role of Vimentin Intermediate Filaments in the Progression of Lung Cancer. *Am. J. Respir. Cell Mol. Biol.* **50**, 1–6

8. Satelli, A., and Li, S. (2011) Vimentin in cancer and its potential as a molecular target for cancer therapy. *Cell. Mol. Life Sci.* **68**, 3033–46

9. Strelkov, S. V, Herrmann, H., Geisler, N., Lustig, A., Ivaninskii, S., Zimbelmann, R., Burkhard, P., and Aebi, U. (2001) Divide-and-conquer crystallographic approach towards an atomic structure of intermediate filaments. *J. Mol. Biol.* **306**, 773–81

10. Strelkov, S. V, Herrmann, H., Geisler, N., Wedig, T., Zimbelmann, R., Aebi, U., and Burkhard, P. (2002) Conserved segments 1A and 2B of the intermediate filament dimer: their atomic structures and role in filament assembly. *EMBO J.* **21**, 1255–66

11. Steinert, P. M., Marekov, L. N., and Parry, D. A. D. (1993) Diversity of intermediate filament structure. Evidence that the alignment of coiled-coil molecules in vimentin is different from that in keratin intermediate filaments. *J. Biol. Chem.* **268**, 24916–24925

12. Hess, J. F., Budamagunta, M. S., Voss, J. C., and FitzGerald, P. G. (2004) Structural characterization of human vimentin rod 1 and the sequencing of assembly steps in intermediate filament formation in vitro using site-directed spin labeling and electron paramagnetic resonance. *J. Biol. Chem.* **279**, 44841–6

13. Chernyatina, A. A., Nicolet, S., Aebi, U., Herrmann, H., and Strelkov, S. V (2012) Atomic structure of the vimentin central α-helical domain and its implications for intermediate filament assembly. *Proc. Natl. Acad. Sci. .* **109**, 13620–13625

14. Aziz, A., Hess, J. F., Budamagunta, M. S., Voss, J. C., Kuzin, A. P., Huang, Y. J., Xiao, R., Montelione, G. T., FitzGerald, P. G., and Hunt, J. F. (2012) The structure of vimentin linker 1 and rod 1B domains characterized by site-directed spin-labeling electron paramagnetic resonance (SDSL-EPR) and X-ray crystallography. *J. Biol. Chem.* **287**, 28349–61

15. Schaffeld, M., Herrmann, H., Schultess, J., and Markl, J. (2001) Vimentin and desmin of a cartilaginous fish, the shark : Sequence, expression patterns and in vitro assembly. *Eur. J. Cell Biol.* **80**, 692–702

16. Chernyatina, A. A., Guzenko, D., and Strelkov, S. V (2015) Intermediate filament structure: the bottom-up approach. *Curr. Opin. Cell Biol.* **32**, 65–72

17. Geisler, N., Kaufmann, E., and Weber, K. (1982) Proteinchemical characterization of three

structurally distinct domains along the protofilament unit of desmin 10 nm filaments. *Cell*. **30**, 277–86

18. Lee, J. H., Richter, W., Namkung, W., Kim, K. H., Kim, E., Conti, M., and Lee, M. G. (2007) Dynamic regulation of cystic fibrosis transmembrane conductance regulator by competitive interactions of molecular adaptors. *J. Biol. Chem.* **282**, 10414–22

19. Herrmann, H., Häner, M., Brettel, M., Müller, S. A., Goldie, K. N., Fedtke, B., Lustig, A., Franke, W. W., and Aebi, U. (1996) Structure and assembly properties of the intermediate filament protein vimentin: the role of its head, rod and tail domains. *J. Mol. Biol.* **264**, 933–53

20. Herrmann, H., Häner, M., Brettel, M., Ku, N. O., and Aebi, U. (1999) Characterization of distinct early assembly units of different intermediate filament proteins. *J. Mol. Biol.* **286**, 1403–20

21. Parry D. A. D., S. P. M. (1995) Intermediate Filament Structure. *Springer-Verlag*

22. Winheim, S., Hieb, A. R., Silbermann, M., Surmann, E.-M., Wedig, T., Herrmann, H., Langowski, J., and Mücke, N. (2011) Deconstructing the late phase of vimentin assembly by total internal reflection fluorescence microscopy (TIRFM). *PLoS One*. **6**, e19202

23. Nöding, B., Herrmann, H., and Köster, S. (2014) Direct observation of subunit exchange along mature vimentin intermediate filaments. *Biophys. J.* **107**, 2923–31

24. Kapinos, L. E., Schumacher, J., Mücke, N., Machaidze, G., Burkhard, P., Aebi, U., Strelkov, S. V, and Herrmann, H. (2010) Characterization of the head-to-tail overlap complexes formed by human lamin A, B1 and B2 "half-minilamin" dimers. *J. Mol. Biol.* **396**, 719–31

25. Marsh, J. J., Guan, H. S., Li, S., Chiles, P. G., Tran, D., and Morris, T. A. (2013) Structural insights into fibrinogen dynamics using amide hydrogen/deuterium exchange mass spectrometry. *Biochemistry*. **52**, 5491–502

26. Kowlessur, D., and Tobacman, L. S. (2012) Significance of troponin dynamics for Ca2+-mediated regulation of contraction and inherited cardiomyopathy. *J. Biol. Chem.* **287**, 42299–311

27. Premchandar, A., Kupniewska, A., Tarnowski, K., Mücke, N., Mauermann, M., Kaus-Drobek, M., Edelman, A., Herrmann, H., and Dadlez, M. (2015) Analysis of distinct molecular assembly complexes of keratin K8 and K18 by hydrogen-deuterium exchange. *J. Struct. Biol.* **192**, 426–440

28. Meier, M., Padilla, G. P., Herrmann, H., Wedig, T., Hergt, M., Patel, T. R., Stetefeld, J., Aebi, U., and Burkhard, P. (2009) Vimentin coil 1A-A molecular switch involved in the initiation of filament elongation. *J. Mol. Biol.* **390**, 245–61

29. Köster, S., Weitz, D. A., Goldman, R. D., Aebi, U., and Herrmann, H. (2015) Intermediate filament mechanics in vitro and in the cell: from coiled coils to filaments, fibers and networks. *Curr. Opin. Cell Biol.* **32**, 82–91

30. Kirmse, R., Portet, S., Mücke, N., Aebi, U., Herrmann, H., and Langowski, J. (2007) A quantitative kinetic model for the in vitro assembly of intermediate filaments from tetrameric vimentin. *J. Biol. Chem.* **282**, 18563–72

31. Herrmann, H., Strelkov, S. V, Feja, B., Rogers, K. R., Brettel, M., Lustig, A., Häner, M., Parry, D. A., Steinert, P. M., Burkhard, P., and Aebi, U. (2000) The intermediate filament protein consensus motif of helix 2B: its atomic structure and contribution to assembly. *J. Mol. Biol.* **298**, 817–32

32. Mücke, N., Kreplak, L., Kirmse, R., Wedig, T., Herrmann, H., Aebi, U., and Langowski, J. (2004) Assessing the flexibility of intermediate filaments by atomic force microscopy. *J. Mol. Biol.* **335**, 1241–50

33. Mücke, N., Wedig, T., Bürer, A., Marekov, L. N., Steinert, P. M., Langowski, J., Aebi, U., and Herrmann, H. (2004) Molecular and biophysical characterization of assembly-starter units of human vimentin. *J. Mol. Biol.* **340**, 97–114

34. Lichtenstern, T., Mücke, N., Aebi, U., Mauermann, M., and Herrmann, H. (2012) Complex formation and kinetics of filament assembly exhibited by the simple epithelial keratins K8 and K18. *J. Struct. Biol.* **177**, 54–62

35. Bär, H., Mücke, N., Ringler, P., Müller, S. A., Kreplak, L., Katus, H. A., Aebi, U., and Herrmann, H. (2006) Impact of disease mutations on the desmin filament assembly process. *J. Mol. Biol.* **360**, 1031–42

36. Nicolet, S., Herrmann, H., Aebi, U., and Strelkov, S. V (2010) Atomic structure of vimentin coil 2. *J. Struct. Biol.* **170**, 369–76

37. Smith, T. A., Strelkov, S. V, Burkhard, P., Aebi, U., and Parry, D. A. D. (2002) Sequence Comparisons of Intermediate Filament Chains: Evidence of a Unique Functional/Structural Role for Coiled-Coil Segment 1A and Linker L1. *J. Struct. Biol.* **137**, 128–145

38. Herrmann, H., and Aebi, U. (1998) Intermediate filament assembly: fibrillogenesis is driven by decisive dimer-dimer interactions. *Curr. Opin. Struct. Biol.* **8**, 177–185

39. Steinert, P. M., Marekov, L. N., Fraser, R. D. B., and Parry, D. A. D. (1993) Keratin Intermediate Filament Structure: Crosslinking Studies Yield Quantitative Information on Molecular Dimensions and Mechanism of Assembly. *J. Mol. Biol.* **230**, 436–452

40. Wu, K. C., Bryan, J. T., Morasso, M. I., Jang, S. I., Lee, J. H., Yang, J. M., Marekov, L. N., Parry, D. A., and Steinert, P. M. (2000) Coiled-coil trigger motifs in the 1B and 2B rod domain segments are required for the stability of keratin intermediate filaments. *Mol. Biol. Cell*. **11**, 3539–58

41. Aziz, A., Hess, J. F., Budamagunta, M. S., Voss, J. C., and Fitzgerald, P. G. (2010) Site-directed spin labeling and electron paramagnetic resonance determination of vimentin head domain structure. *J. Biol. Chem.* **285**, 15278–85

42. Herrmann, H., and Aebi, U. (2004) INTERMEDIATE FILAMENTS: Molecular Structure, Assembly Mechanism, and Integration Into Functionally Distinct Intracellular Scaffolds. *Annu. Rev. Biochem.* **73**, 749–789

43. Izawa, I., and Inagaki, M. (2006) Regulatory mechanisms and functions of intermediate filaments: A study using site- and phosphorylation state-specific antibodies. *Cancer Sci.* **97**, 167–174

44. Parry, D. A. D. (2006) Hendecad repeat in segment 2A and linker L2 of intermediate filament chains implies the possibility of a right-handed coiled-coil structure. *J. Struct. Biol.* **155**, 370–4

45. Hess, J. F., Budamagunta, M. S., Shipman, R. L., FitzGerald, P. G., and Voss, J. C. (2006) Characterization of the linker 2 region in human vimentin using site-directed spin labeling and electron paramagnetic resonance. *Biochemistry*. **45**, 11737–43

46. Parry, D. A. D., Strelkov, S. V, Burkhard, P., Aebi, U., and Herrmann, H. (2007) Towards a molecular description of intermediate filament structure and assembly. *Exp. Cell Res.* **313**, 2204–16

47. Sokolova, A. V, Kreplak, L., Wedig, T., Mücke, N., Svergun, D. I., Herrmann, H., Aebi, U., and Strelkov, S. V (2006) Monitoring intermediate filament assembly by small-angle x-ray scattering reveals the molecular architecture of assembly intermediates. *Proc. Natl. Acad. Sci. U. S. A.* **103**, 16206–11

48. Strelkov, S. V, Schumacher, J., Burkhard, P., Aebi, U., and Herrmann, H. (2004) Crystal structure of the human lamin A coil 2B dimer: implications for the head-to-tail association of nuclear lamins. *J. Mol. Biol.* **343**, 1067–80

49. Herrmann, H., Kreplak, L., and Aebi, U. (2004) Isolation, characterization, and in vitro assembly of intermediate filaments. *Methods Cell Biol.* **78**, 3–24

50. Sitkiewicz, E., Tarnowski, K., Poznański, J., Kulma, M., and Dadlez, M. (2013) Oligomerization interface of RAGE receptor revealed by MS-monitored hydrogen deuterium exchange. *PLoS One*. **8**, e76353

51. Richter, M. M., Poznanski, J., Zdziarska, A., Czarnocki-Cieciura, M., Lipinszki, Z., Dadlez, M., Glover, D. M., and Przewloka, M. R. (2016) Network of protein interactions within the Drosophila inner kinetochore. *Open Biol.* **6**, 150238

FIGURE LEGENDS

FIGURE 1. Domain organization of vimentin monomer and tetramer. *A*, domain classification in a vimentin monomer based on α-helicity structure prediction and X-ray crystal structure data. The α-helical regions are boxed. Those α-helical segments that form coiled coils (coil 1A, coil 1B, coil 2) are in yellow. The α-helical segments that do not form coiled coils are in orange – in particular, the pre-coil domain (*pcd*), and the parallel α-helix–forming segments of coil 2, also referred to as paired bundle (*pb*) (13, 16). For ease of understanding, we refer to this segment as coil 2A and the remainder of coil 2 as coil 2B in the entire text. Non–α-helical N-terminal (head) and C-terminal (tail) domains as well as linkers L1 and L12 are represented by thick black lines. Numbers below the boxes indicate the limits of the individual domains. *B*, model depicting the association of two dimers within a tetramer by the anti-parallel overlap of two dimers via the coil 1 domain. This arrangement of two dimers is referred to as A_{11} alignment. The arrows mark the position of glutamic acid 191, which is in the center of the tetramer model as derived by X-ray crystallography (13). *C*, analytical ultracentrifugation of soluble complexes formed at low ionic strength by wild-type vimentin (wt) and four mutant vimentins (Y117L, Y117S, Y400L, and Y400S). *a*, *b*, sedimentation velocity runs of (a) wt, Y117L, and Y117S vimentins and (b) wt, Y400L, and Y400S vimentins. *c*, Sedimentation equilibrium centrifugation analysis of wt, Y117L, and Y117S vimentins. The data for the individual proteins are color coded as indicated in each panel. *D*, analytical ultracentrifugation of soluble complexes formed in assembly buffer (2 mM NaPi, pH 7.5, 100 mM KCl) by Y117L (left panel) and Y117S (right panel). Sedimentation velocity runs of oligomers assembled at standard conditions (open symbols) and assembled first at high concentration and then diluted tenfold, analogous to the procedure applied in HDex analysis (filled symbols). *E*, electron microscopy of assembled Y117S vimentin. After 1 h of incubation in assembly buffer, the sample was briefly fixed with 0.2% glutaraldehyde in solution, applied to a glow-discharged copper EM grid, and negatively stained with uranyl acetate. Bar: 50 nm.

FIGURE 2. Identification of contact sites in tetramers and filaments of vimentin. *A*, *B*, % deuteration of amide protons in all identified peptides obtained under (A) low and (B) high ionic strength conditions. Tetramers are encountered in low ionic strength conditions and filaments in high ionic strength conditions. As established in Figure 1, coiled-coil forming domains are marked with yellow, and the *pcd* and coil 2A by orange rectangles. Y-axis error bars denote standard deviations calculated from three independent experiments. *C*, the difference in the fraction of exchanged amide protons between tetramers and filaments. Error bars were calculated as the square root of the sum of variances of the subtracted data points. In A–C, the position of the peptide in the sequence is shown on the horizontal axis represented by a bar with the length equal to that of the peptide. In A–D, the vertical axis marks the fraction exchanged after 10 s (black) and 20 min (red). Shorter incubation time (10 s) best characterizes the exchange in more flexible regions while longer one (20 min) in more stable regions. *D*, a schematic representation of differences in deuteration between tetramers and filaments. Only those regions of interest with over 10% difference in deuteration and a p-value score below 0.01 on the Student's t-test (marked with asterisks) are shown in the scheme.

FIGURE 3. Analysis of a large fragment of vimentin that remained undigested during the brief pepsin proteolysis step preceding the HDexMS measurements. *A*, the isotopic envelope detected in the wtVim analysis, corresponding to the average peptide mass of 12899.00 Da, close to the mass 12899.29 Da expected for the $S_{299}EA…GEE_{408}$ peptide, covering coil 2B of vimentin. Isotopic envelopes before the exchange (panel (i)), at different stages of exchange in the tetrameric and filamentous state (panels (ii)−(v)), and for full exchange (panel (vi)) are shown. *B*, The fragment of a molecular mass larger than 10 kDa was also detected in PAGE gels after on-line digestion of wtVim on a pepsin resin (panel B, lane 6) preceding the MS analysis. In vimentin variants in which Y400 was substituted by a different amino acid, this fragment was not present (panel A − lane (vii)). Instead, in these mutants fragments of different masses, corresponding to different coil 2 regions, were detected. *C*, The table shows the values of the detected and expected masses of these fragments. Y400L mutation leads to a fragment larger by 10 amino acids and

mutation Y400S to a smaller fragment. In Y400F, a slow assembling, filament-forming mutant of vimentin, the site of proteolysis remains the same as in wtVim.

FIGURE 4. Identification of contact sites in octamers and ULFs of Y117L vimentin. *A*, *B*, % deuteration of amide protons in all identified peptides obtained under (A) low and (B) high ionic strength conditions. Octamers are encountered in low ionic strength conditions and ULFs in high ionic strength conditions. As established in Figure 1, coiled-coil–forming domains are marked with yellow, and the *pcd* and coil 2A by orange rectangles. Y-axis error bars denote standard deviations calculated from three independent experiments. *C*, the difference in the fraction of exchanged amide protons between octamers and ULFs. Error bars were calculated as the square root of the sum of variances of the subtracted data points. In A–C, the position of the peptide in the sequence is shown on the horizontal axis represented by a bar with the length equal to that of the peptide. In A–D, the vertical axis marks the fraction exchanged after 10 s (black) and 20 min (red). The shorter incubation time (10 s) best characterizes the exchange in more flexible regions while the longer one (20 min) best characterizes the more stable regions. *D*, a schematic representation of differences in deuteration between octamers and ULFs. Only those regions of interest with over 10% difference in deuteration and a p-value score below 0.01 on the Student's t-test (marked with asterisks) are shown in the scheme.

FIGURE 5. Schematic representation of the differences in deuteration of wild-type vimentin and the Y117L and Y117S vimentin mutants. *A*, wtVim$_{Tet}$ *vs.* Y117L$_{Oct}$; *B*, wtVim$_{Tet}$ *vs.* Y117L$_{ULF}$; *C*, Y117L$_{ULF}$ *vs.* wtVim$_{Fil}$; *D*, wtVim$_{Tet}$ *vs.* Y117S$_{Tet}$; *E*, wtVim$_{Tet}$ *vs.* Y117S$_{ULF}$; *F*, Y117S$_{ULF}$ *vs.* wtVim$_{Fil}$. Black bars indicate the difference after 10 s of incubation and the red bars the difference after 20 min. Shorter incubation time (10 s) best characterizes the exchange in more flexible regions while the longer time (20 min) best characterizes more stable regions. Only those regions of interest with over 10% difference in deuteration and a p-value score below 0.01 on the Student's t-test (marked with asterisks) are shown in the scheme.

FIGURE 6. Time-dependent mass shift patterns after deuteration in the peptide containing the conserved tyrosine at position 117. The isotopic envelopes of the Q$_{108}$ELNDRFANX$_{117}$ peptide in wtVim, and the two Y117 vimentin mutants. X stands for Tyr in wtVim, Leu in Y117L, and Ser in Y117S. Note that the 10 s and 20 min time points correspond to the analysis shown in Figures 4 and 5. The pattern of exchange in the peptide can be followed through the unexchanged (0 s) to the fully exchanged (24 h) state.

FIGURE 7. Schematic representation of the differences in deuteration of wild-type vimentin and the Y400L and Y400S vimentin mutants. *A*, Y400L$_{Tet}$ *vs.* Y400L$_{ULF}$; *B*, wtVim$_{Tet}$ *vs.* Y400L$_{Tet}$; *C*, Y117L$_{ULF}$ *vs.* Y400L$_{ULF}$; *D*, Y400S$_{Tet}$ *vs.* Y400S$_{ULF}$; *E*, wtVim$_{Tet}$ *vs.* Y400S$_{ULF}$; *F*, Y117S$_{ULF}$ *vs.* Y400S$_{ULF}$. Black bars indicate the difference after 10 s of incubation and the red bars the difference after 20 min. The shorter incubation time (10 s) best characterizes the exchange in more flexible regions while the longer one (20 min) best characterizes more stable regions. Only those regions of interest with over 10% difference in deuteration and a p-value score below 0.01 on the Student's t-test (marked with asterisks) are shown in the scheme. The change in coil 1A passes the t-test p-value cutoff of 0.05.

FIGURE 8. Circular dichroism (CD) spectroscopic analysis of different vimentin peptides. The following three peptides covering coiled-coil contact regions were analyzed: peptide 1A, peptide 2A, and peptide 2B. *A*, CD spectra for 1A (black), a mixture of 1A with 2A (1A–2A, blue), and a mixture of 1A with 2A and 2B (1A–2A–2B, red), at 100 µM (solid line) and 8.8 µM (dash-dot line). *B*, the concentration dependence of the mean residue ellipticity at 222 nm for 1A (black), 1A–2A (blue), and 1A–2A–2B (red) are shown. While the signal for 1A is the strongest at the highest concentration, it becomes the weakest at low concentration. *C*, the measured concentration dependence of molar ellipticity at 222 nm for 1A (black), 2A (light blue), 2B (purple), and their mixtures—1A–2A (dark blue) and 1A–2A–2B (red)—is compared with the arithmetic sum of signals of the components in the mixture, namely 1A+2A (dash-dot blue line) or

22

1A2A+2B (dash-dot red line). The difference between the measured and calculated values indicates the non-additivity effect and heterooligomerization of the peptides.

FIGURE 9. Model of a cross-coiled organization of vimentin oligomeric states. *A*, a molecular model of the coil 1A–coil 2A antiparallel heterotetramer, based on the overlay of coil 1A 3S4R X-ray structure (green trace) on one of the two 2A dimers in a non-native 3KLT homotetramer of coils 2A (blue trace), shown as a simplified scheme (upper panel) and as an X-ray structure overlay (lower panel). Residues typically assigned to coiled-coil positions *a-d-h* are highlighted yellow in 3KLT and positions *a-d* in orange in 3S4R. When 1A and 2A segments originate from different tetramers, these tetramers become cross-coiled, enabling stabilization of higher order oligomers (as described in Figure 10). *B*, the cross-coiled coil 1A–2A heterotetramer, shown in panel A, overlaid on the 3UF1 X-ray structure of the coil 1B tetramer (red trace). The upper panel illustrates the overlay procedure in a schematic way, with two coil 1A–2A tetramers merged into one coil 1B tetramer by concatenation of coil 1B helices present both in 3S4R and 3UF1 at CA coordinates of residues 149–189. Arrows mark the location of residues 149 and 189 in both 3S4R and 3UF1. Note that the coil 2 and coil 1 segments do not have to come from the same tetramer, as described schematically in Figure 10.

FIGURE 10. Possible inter-tetrameric connectivities network linking tetramers into octamers. *A*, the scheme assuming the cross-coiling *via* coil 1A–coil 2A complex shown in Figure 9. Thick rectangles indicate helical regions of high stability, thin rectangles indicate helical regions of low stability, as measured by HDex, and lines indicate flexible linkers. To form an octamer, one of the two coil 1A segments available in each tetramer combines with one of the two coil 2A segments of a different tetramer. This leaves the remaining coil 1A and 2A segments free to participate in inter-octameric interactions, providing the possibility of further lateral growth and circularization to ULF. To form an ULF in a 32-meric oligomer, the linear structure may be circularized by combining the 2A and 1A segments of the flanking tetramers. In all structures, tetramers are linked by flexible L12 linkers, providing structure malleability and ability to rearrange at the compaction step. Circled detail is shown in panel B. *B*, molecular dynamics snapshot showing the detail of the model structure of the coil 1A–coil 2A complex, focusing on the linker L12 trajectory and the network of salt bridges between highly conserved charged residues of the L12 C-terminus (Table 1), with highly conserved charged residues of the L1–coil 1B interface. Four salt bridges are indicated by 3D arrows, namely Asp 264 (L12, chain C, D) – Arg 145 (L1, chain A, B), Red; Lys 262 (L12, chain C, D) – Glu 153 (coil 1B, chain A, B), Magenta.

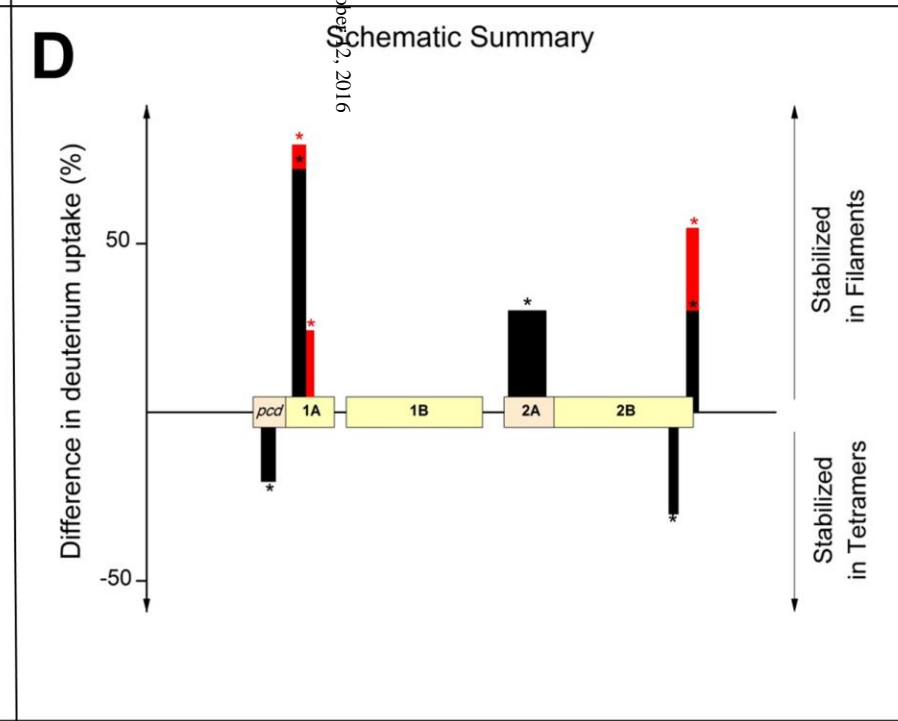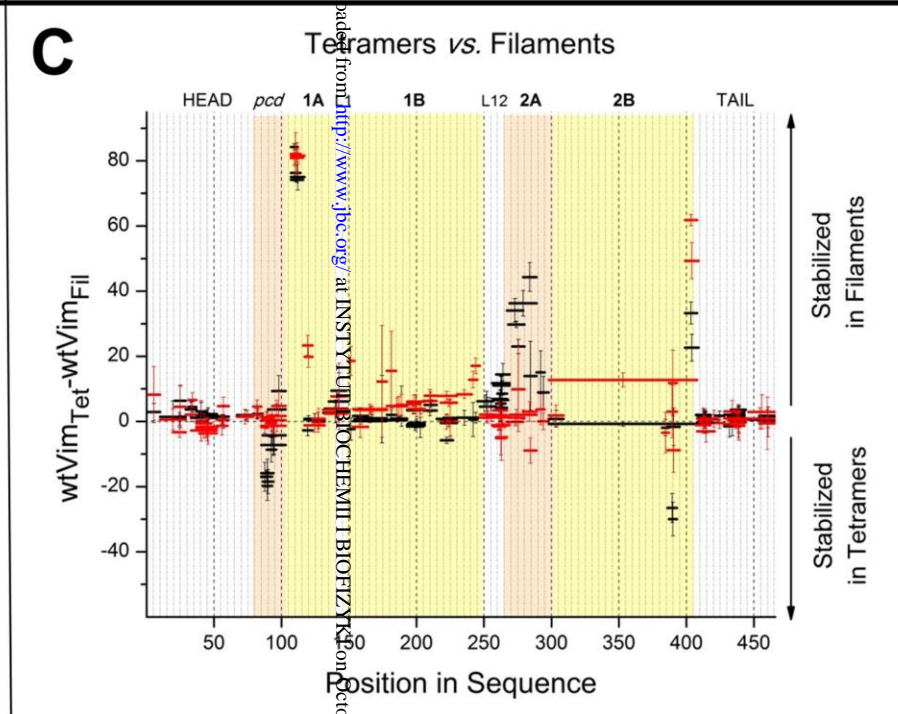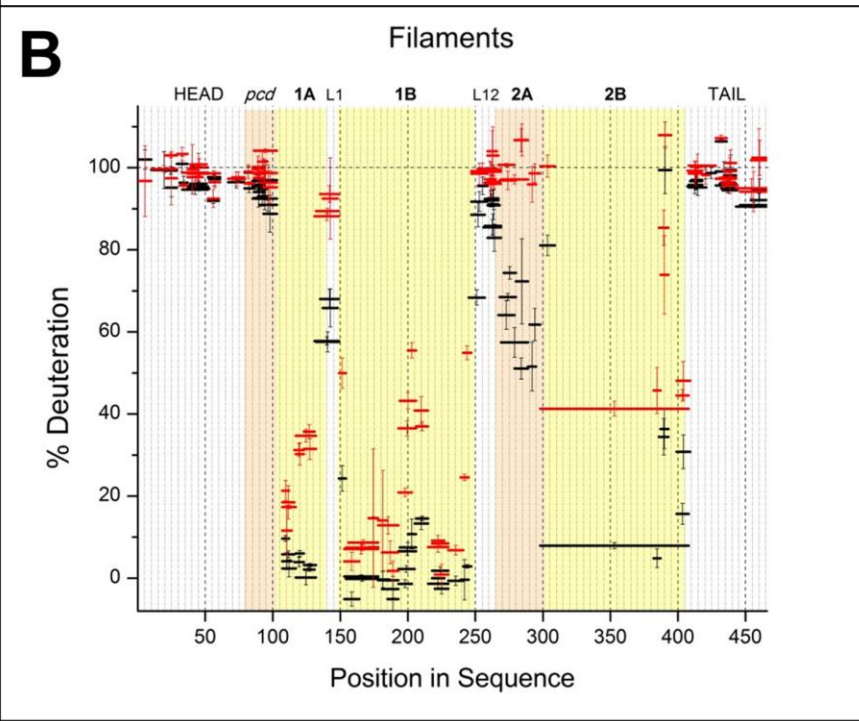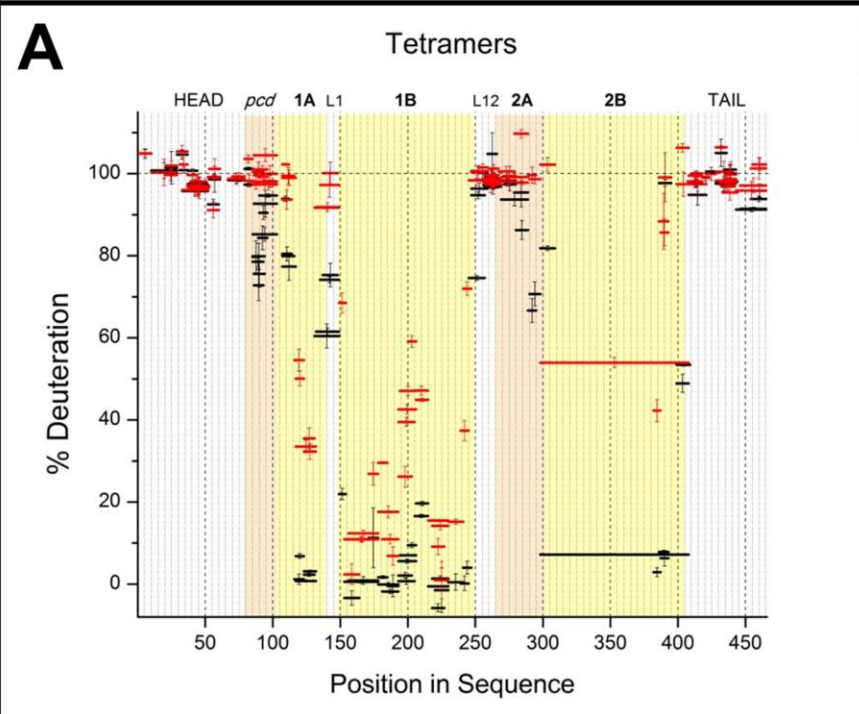**SUPPLEMENTARY MATERIAL**
SUPPLEMENTARY MOVIE S1: Overlay of two alternative models of Coil 1A–2A heterotetramers obtained based on available X-ray structures of vimentin fragments as described in Materials and Methods. Blue marks the coil 2A dimer originating from the PDB:3KLT structure of the fragment $_{264}$D-K$_{334}$, green indicates the coil 1A dimer originating from the PDB:3G1E structure of the fragment $_{102}$N-L$_{138}$, and gray marks the model obtained by homology modeling based on all available structures. Residues typically assigned to coiled-coil positions *a-d-h* are highlighted yellow in 3KLT and positions *a-d* are highlighted orange in 3G1E.
SUPPLEMENTARY MOVIE S2: Overlay of succeeding 1 ns snapshots of the molecular dynamics trajectory for the Coil 1A–2A heterotetramer model based on coil 2A PDB:3KLT structure (blue dimer) and coil 1A PDB:3G1E structure (green dimer). The figure illustrates the stable organization of the heterotetramer core.
SUPPLEMENTARY MOVIE S3: The snapshot of the molecular dynamics trajectory of the coil 1A–2A tetramer in which the sequences were elongated to encompass the L12 linker (cyan). The L1 linker is light green and surrounded by the molecular surface. The coil 1A region is green, while coil 2A is blue. The proposed scheme of the pairing of the two tetramers *via* 1A–2A tetramer (Figure 10) requires that two coil 1A helices of one tetramer laterally approach a different tetramer and dock over its coil 2A dimer. This

23

leaves the two L12 linkers on one side of the heterotetramer, as illustrated by the MD snapshot. It shows the possible conformation in which one of the two L12 linkers passes between the two L1 linkers. A conserved Pro 263 seems crucial for the proposed conformation minimizing the steric clashes, and the L12–L1 crossing is additionally stabilized by salt bridges of conserved clusters of oppositely charged residues (see Table 1). Four salt bridges are indicated by 3D arrows, namely Asp 264 (L12, chain C, D) – Arg 145 (L1, chain A, B), Red; Lys 262 (L12, chain C, D) – Glu 153 (coil 1B, chain A, B), Magenta.

Figure 1
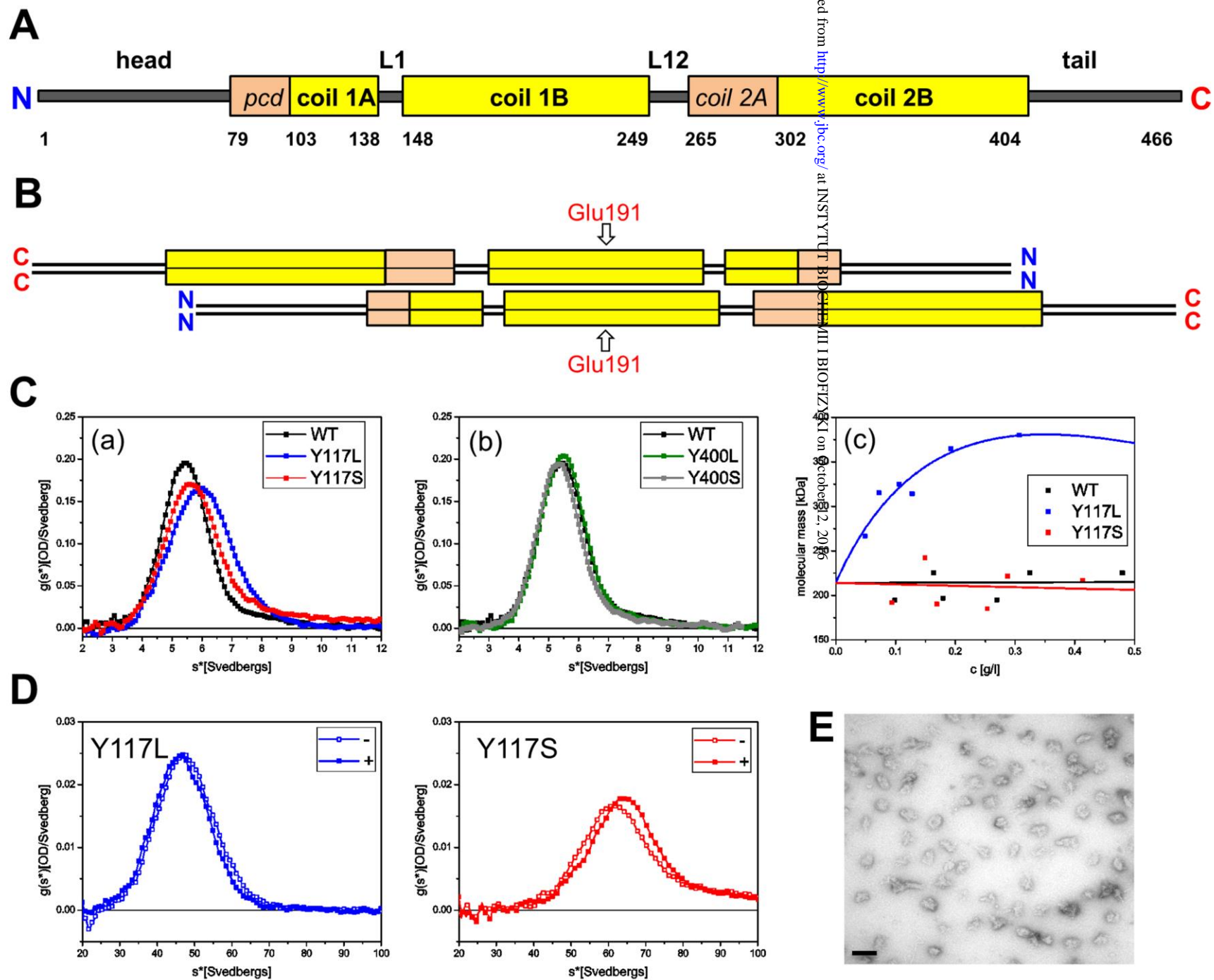
Figure 2

Figure 3

A (spectra, m/z axis from ~1434 to ~1442)

- (vii) Y400L$_{IN}^{0s}$
- (vi) wtVim$_{MAX}^{24h}$
- (v) wtVim$_{Fil}^{20min}$
- (iv) wtVim$_{Fil}^{10s}$
- (iii) wtVim$_{Tet}^{20min}$
- (ii) wtVim$_{Tet}^{10s}$
- (i) wtVim$_{IN}^{0s}$

B (gel with lanes M, 1, 2, 3, 4, 5, 6; markers 75, 50, 37, 25, 20, 15, 10, 5, 2 kDa)
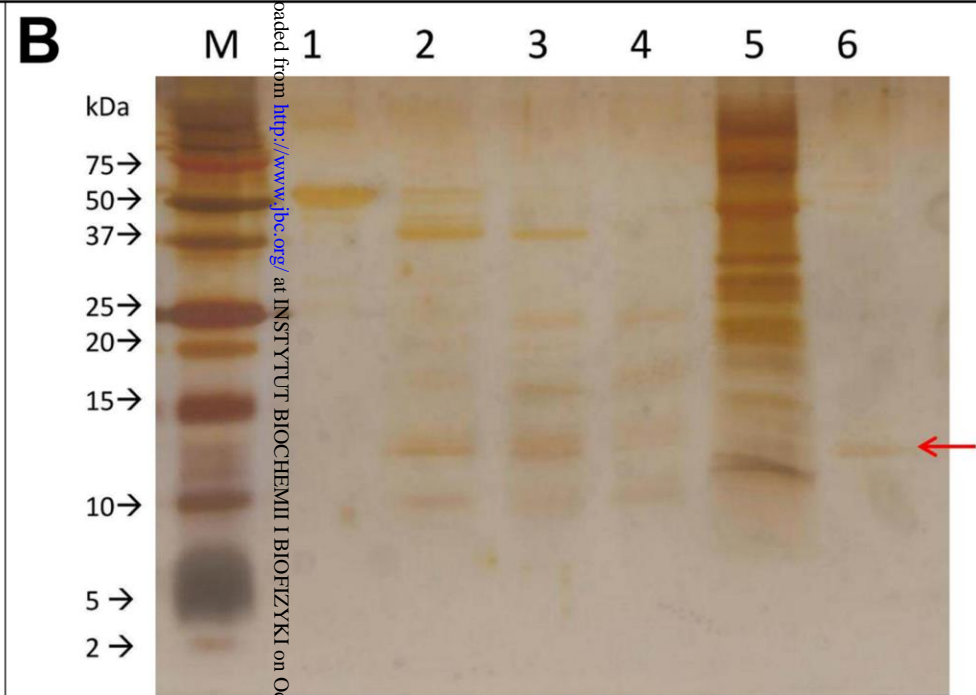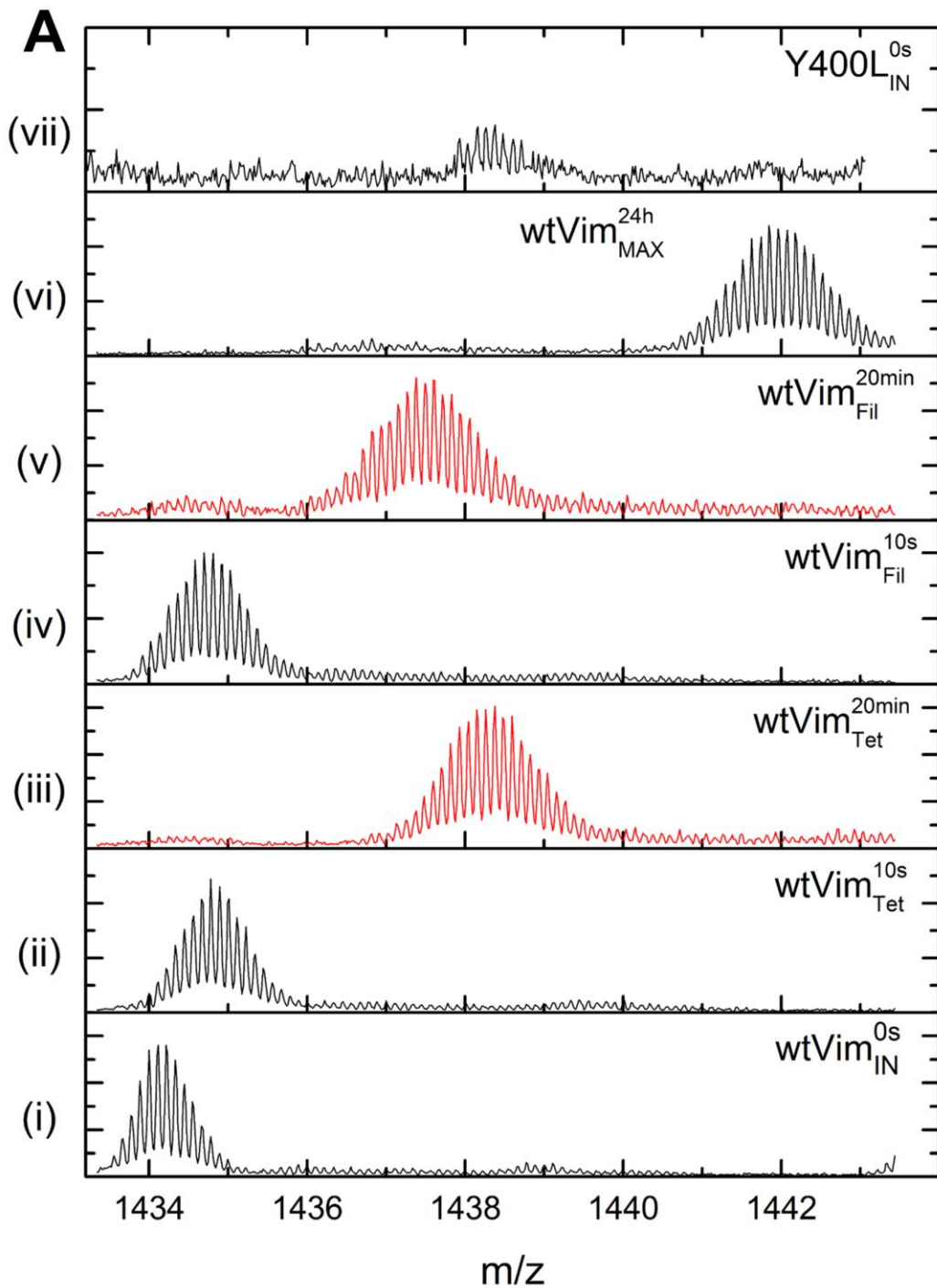
C

Protein	Mass	DB Mass	Δmass (Da)	Sequence	Position
wtVim	12899.000	12899.291	0.291	SEAANRNNDALRQAKQESTEYRRQVQSLTCEVDALKGTNESLERQMREMEENFAVEAANYQDTIGRLQDEIQNMKEEMARHLREYQDLLNVKMALDIEIATYRKLLEGEE	299-408
Y400L	13974.000	13974.610	0.610	SEAANRNNDALRQAKQESTEYRRQVQSLTCEVDALKGTNESLERQMREMEENFAVEAANYQDTIGRLQDEIQNMKEEMARHLREYQDLLNVKMALDIEIATLRKLLEGEESRISLPLPNF	299-418
Y400S	9848.000	9848.774	0.774	SEAANRNNDALRQAKQESTEYRRQVQSLTCEVDALKGTNESLERQMREMEENFAVEAANYQDTIGRLQDEIQNMKEEMAR HLRE	299-382
Y400F	12883.000	12883.292	0.291	SEAANRNNDALRQAKQESTEYRRQVQSLTCEVDALKGTNESLERQMREMEENFAVEAANYQDTIGRLQDEIQNMKEEMARHLREYQDLLNVKMALDIEIATFRKLLEGEE	299-408
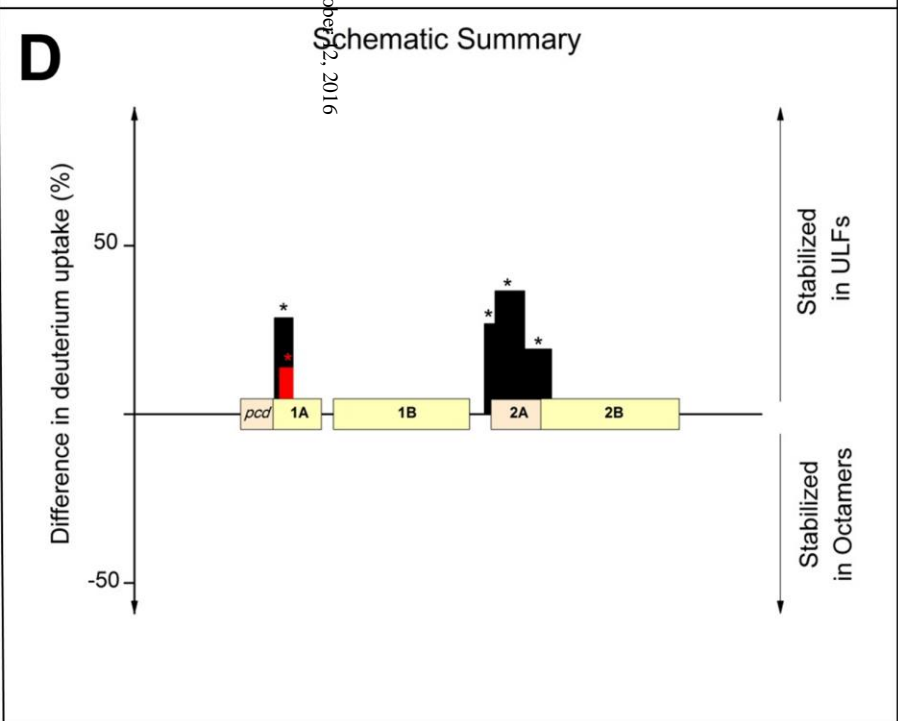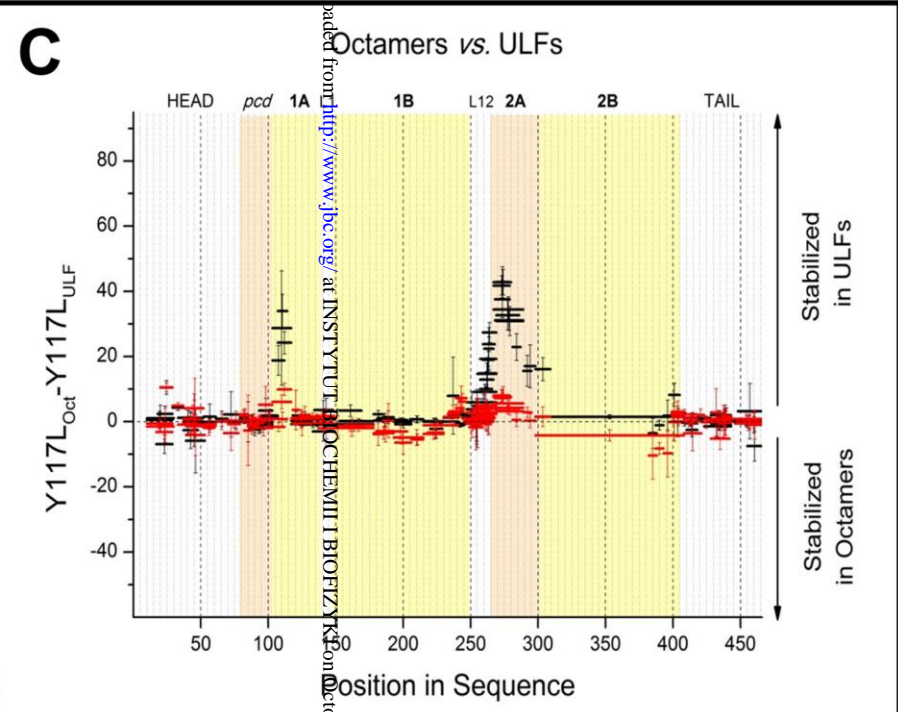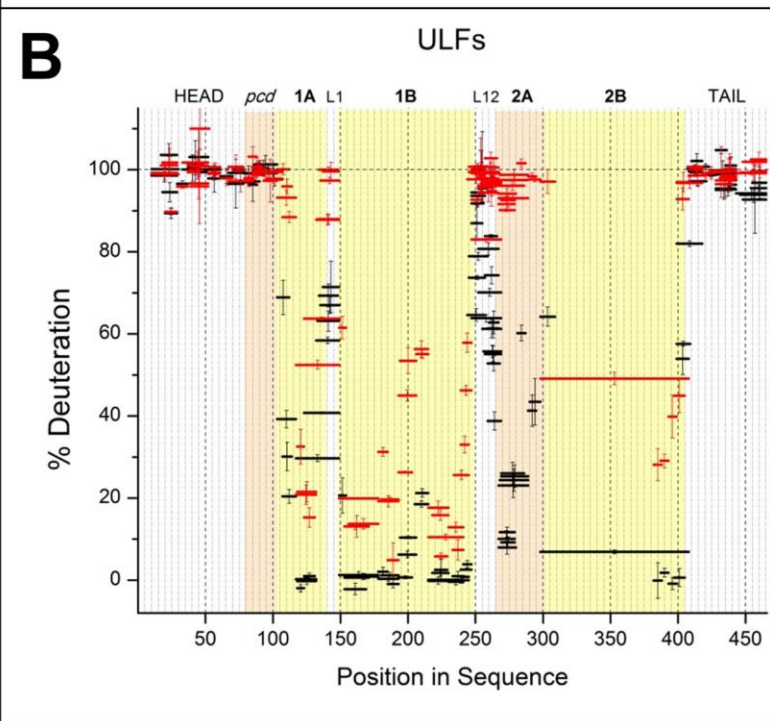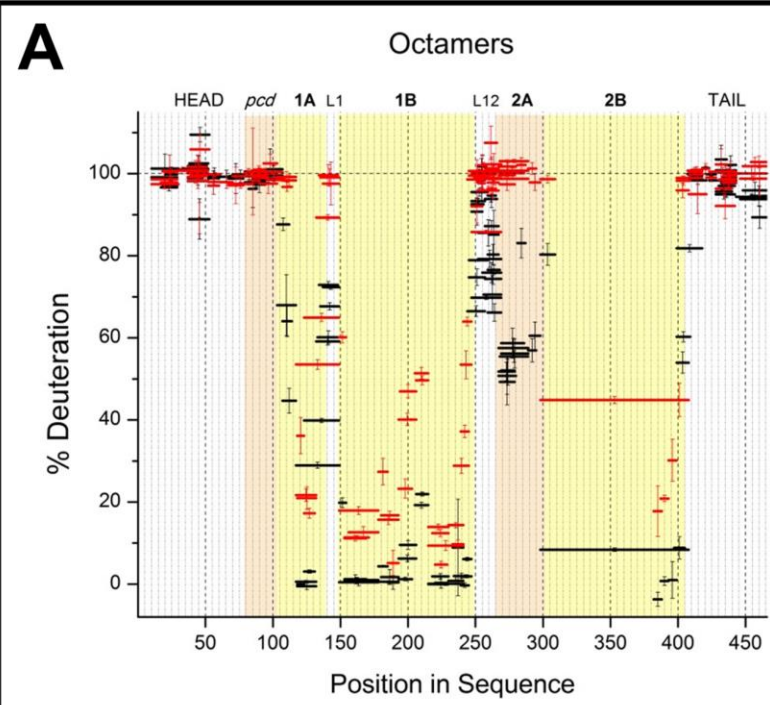
Figure 4

Figure 5

Figure 6

Figure 7

Figure 8

Figure 9

A

Coil 1A region   Coil 2A region   Coil 1A – 2A tetramer

Thr$_{99}$-Leu$_{189}$
parallel dimer

Asp$_{264}$-Asn$_{305}$
tetramer

B

Coil 1A-2A
tetramer

Coil 1B region

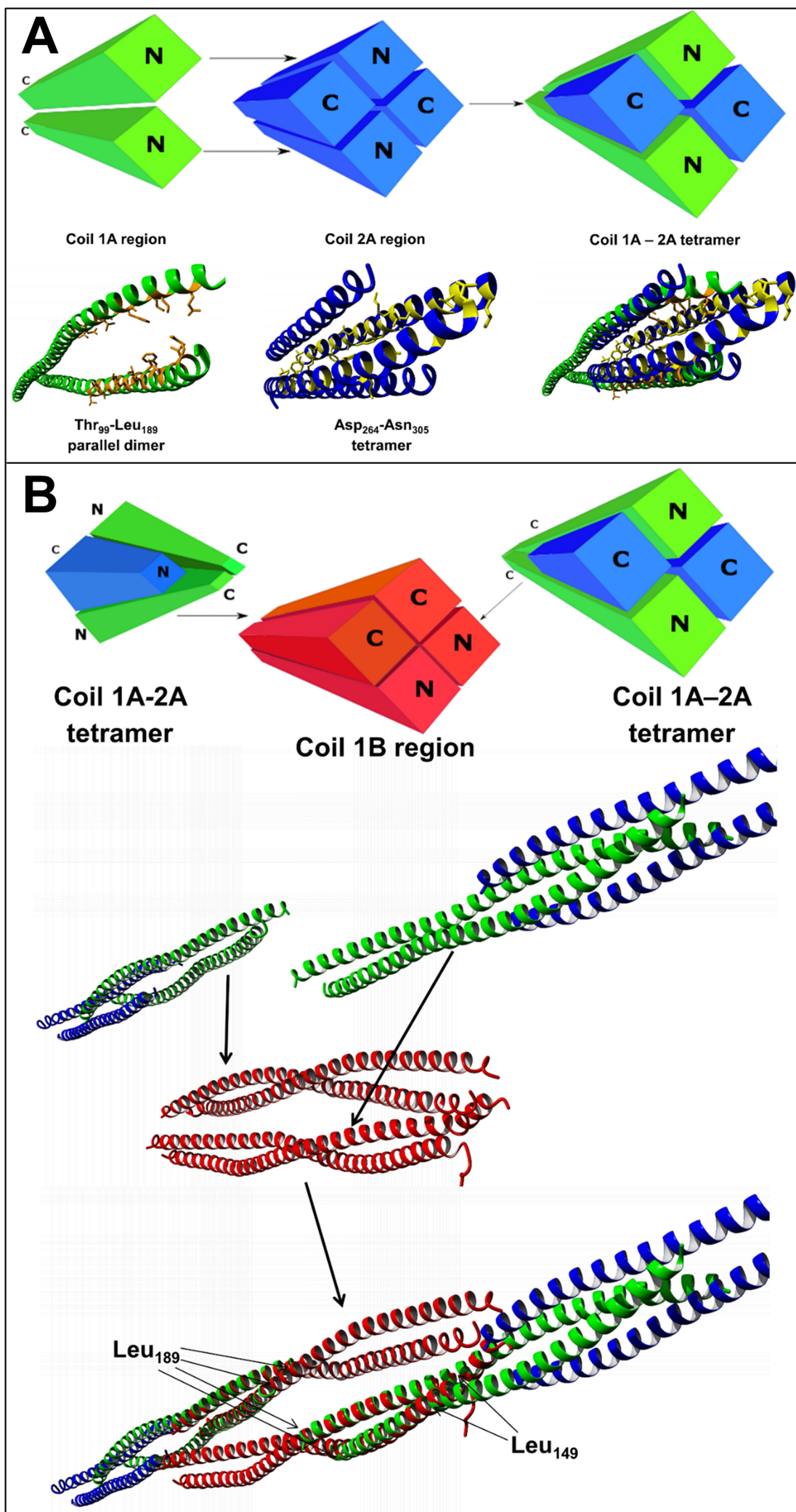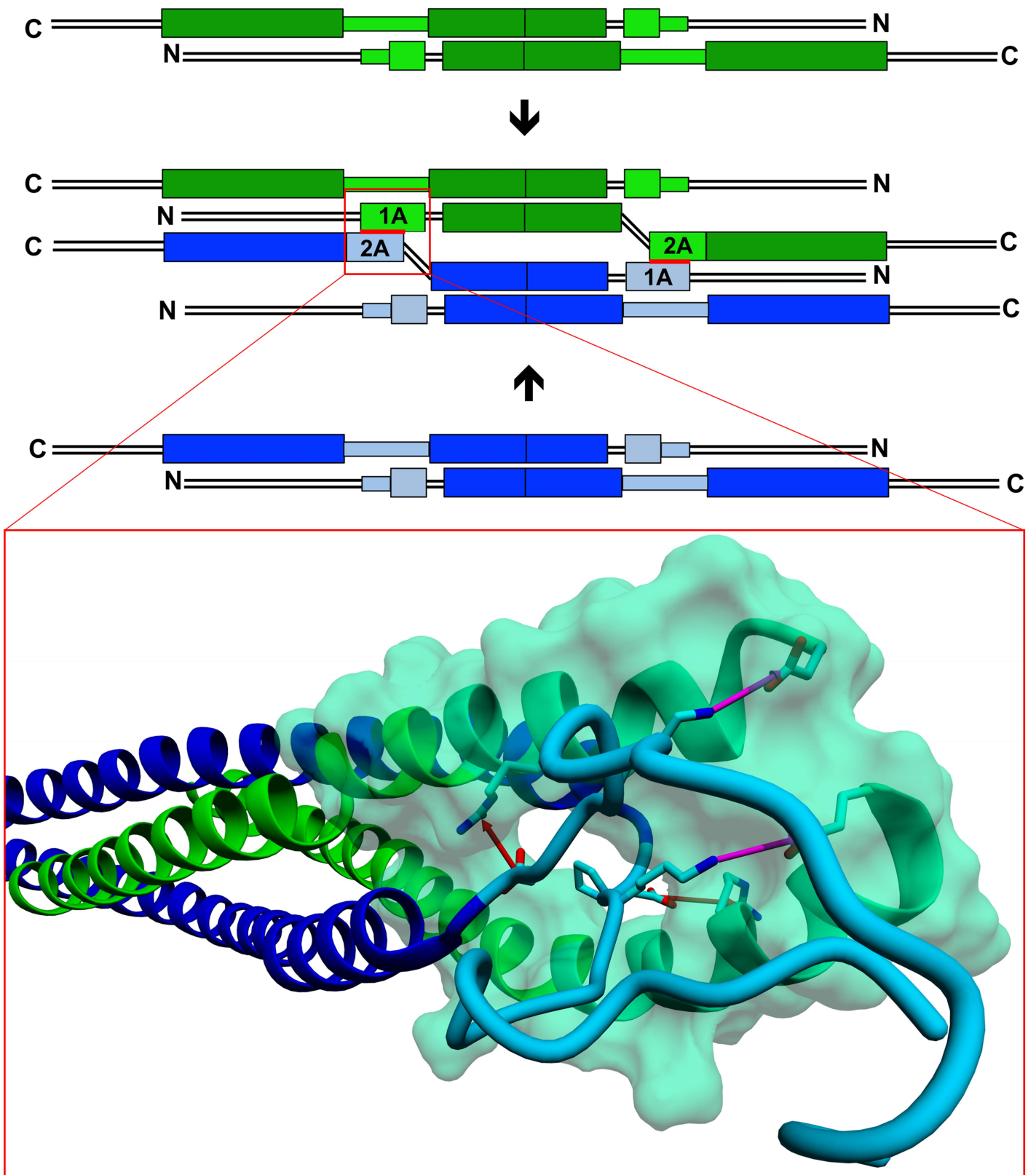Coil 1A–2A
tetramer

Leu$_{189}$

Leu$_{149}$
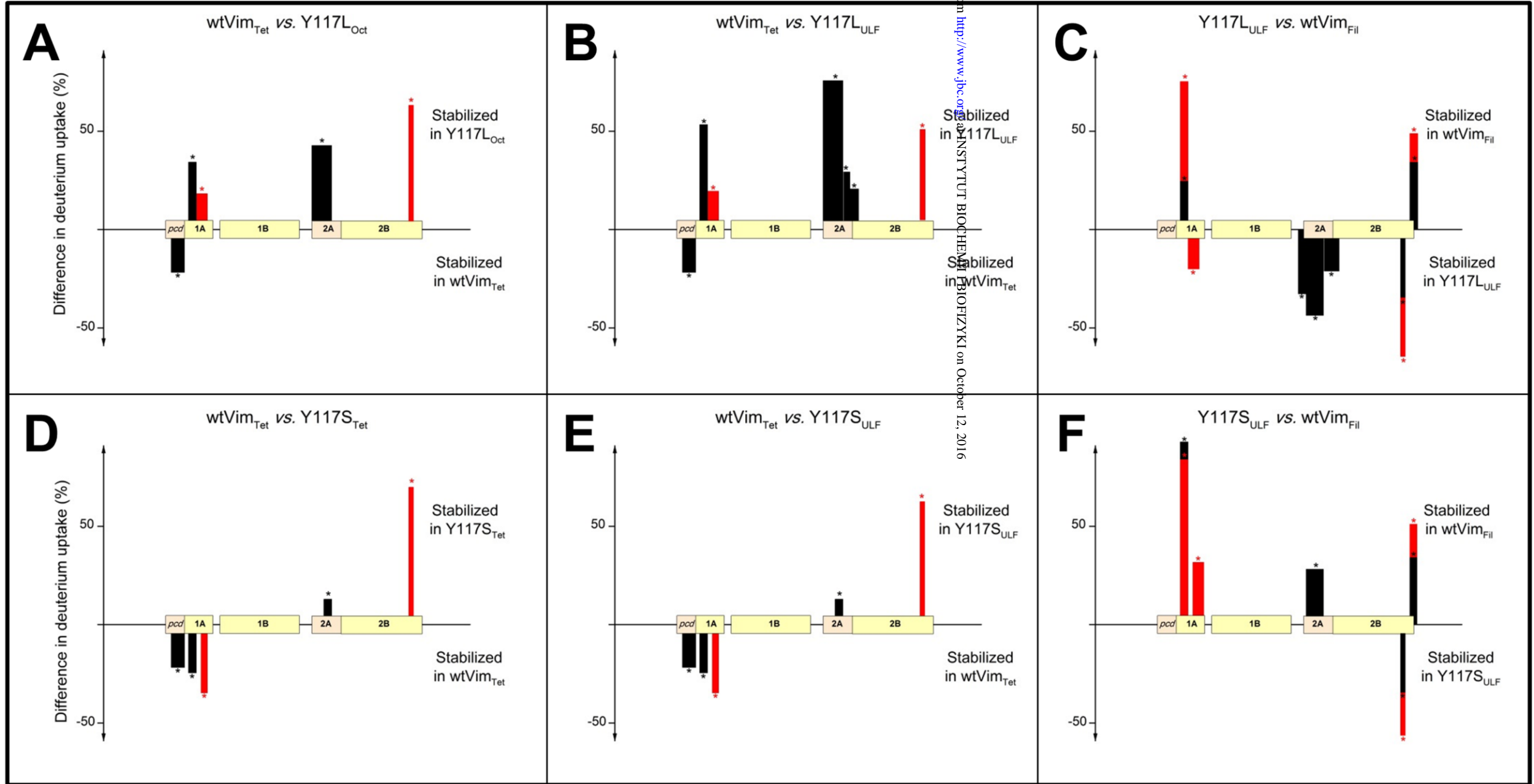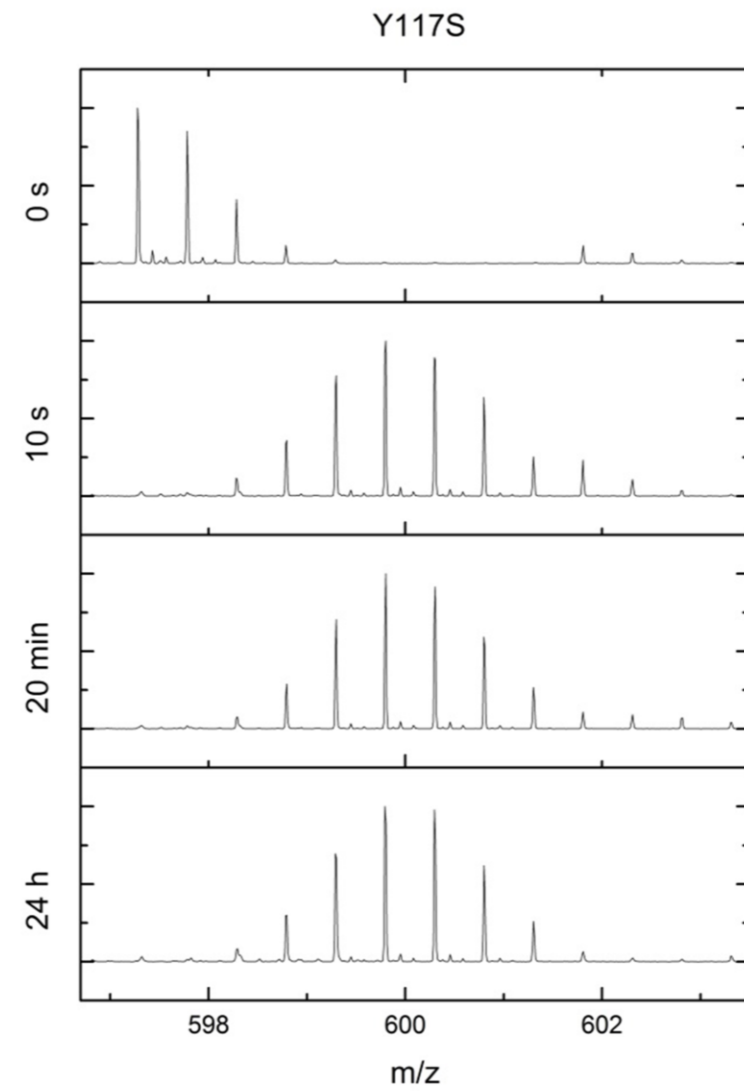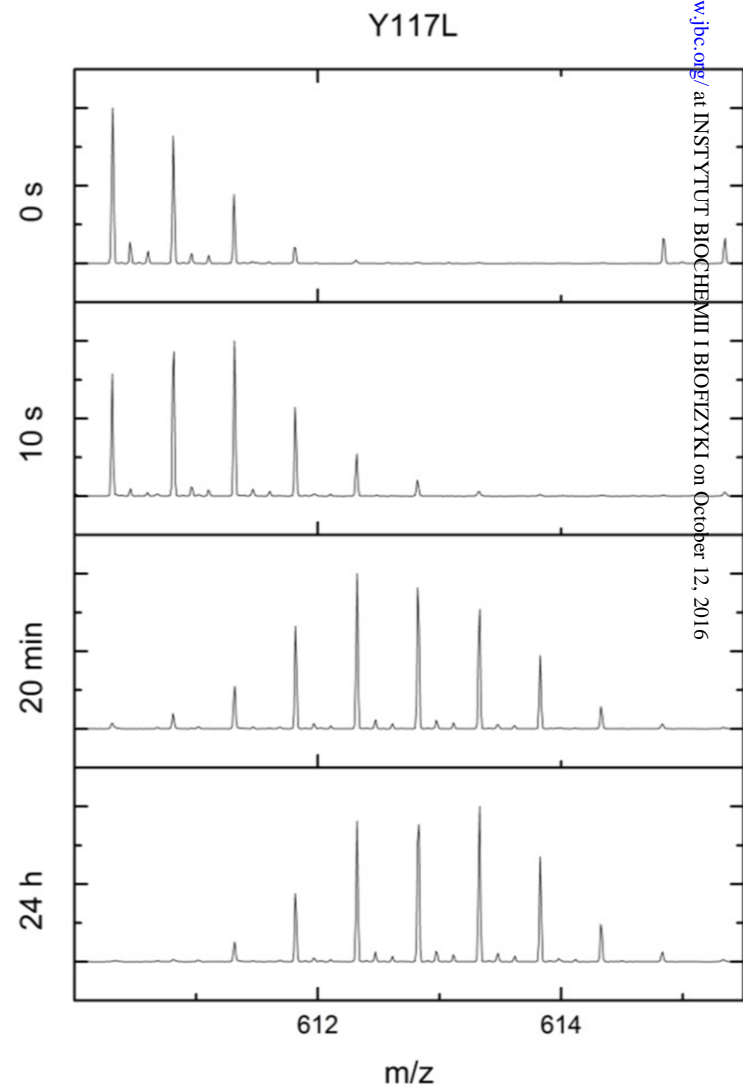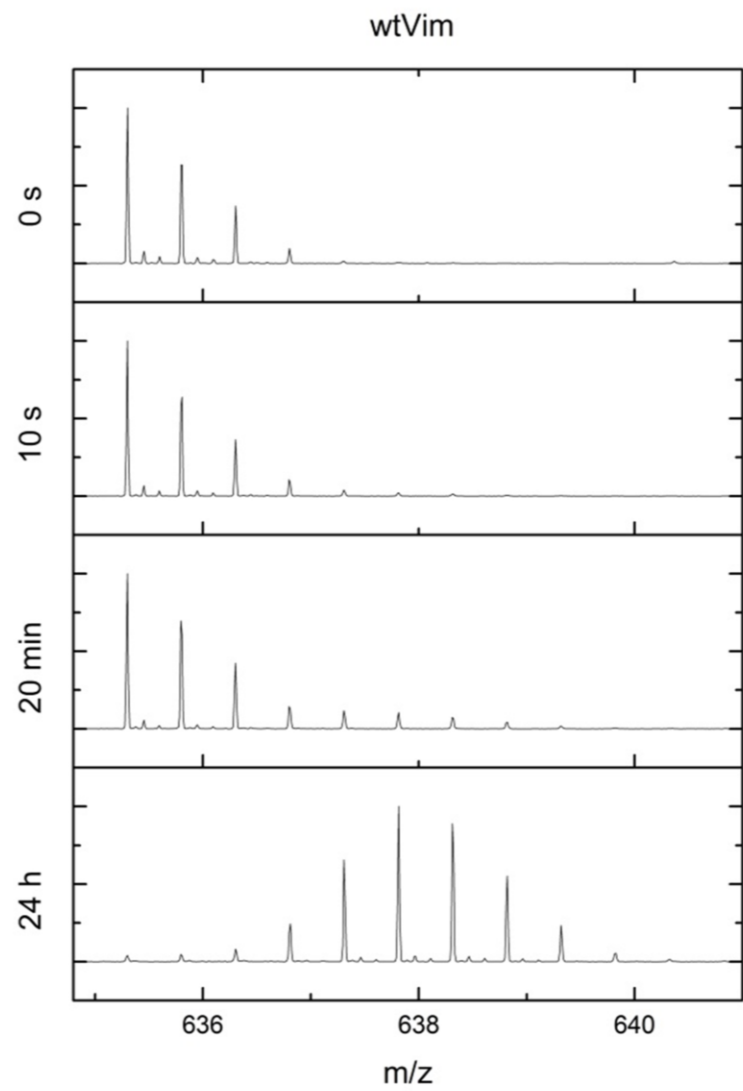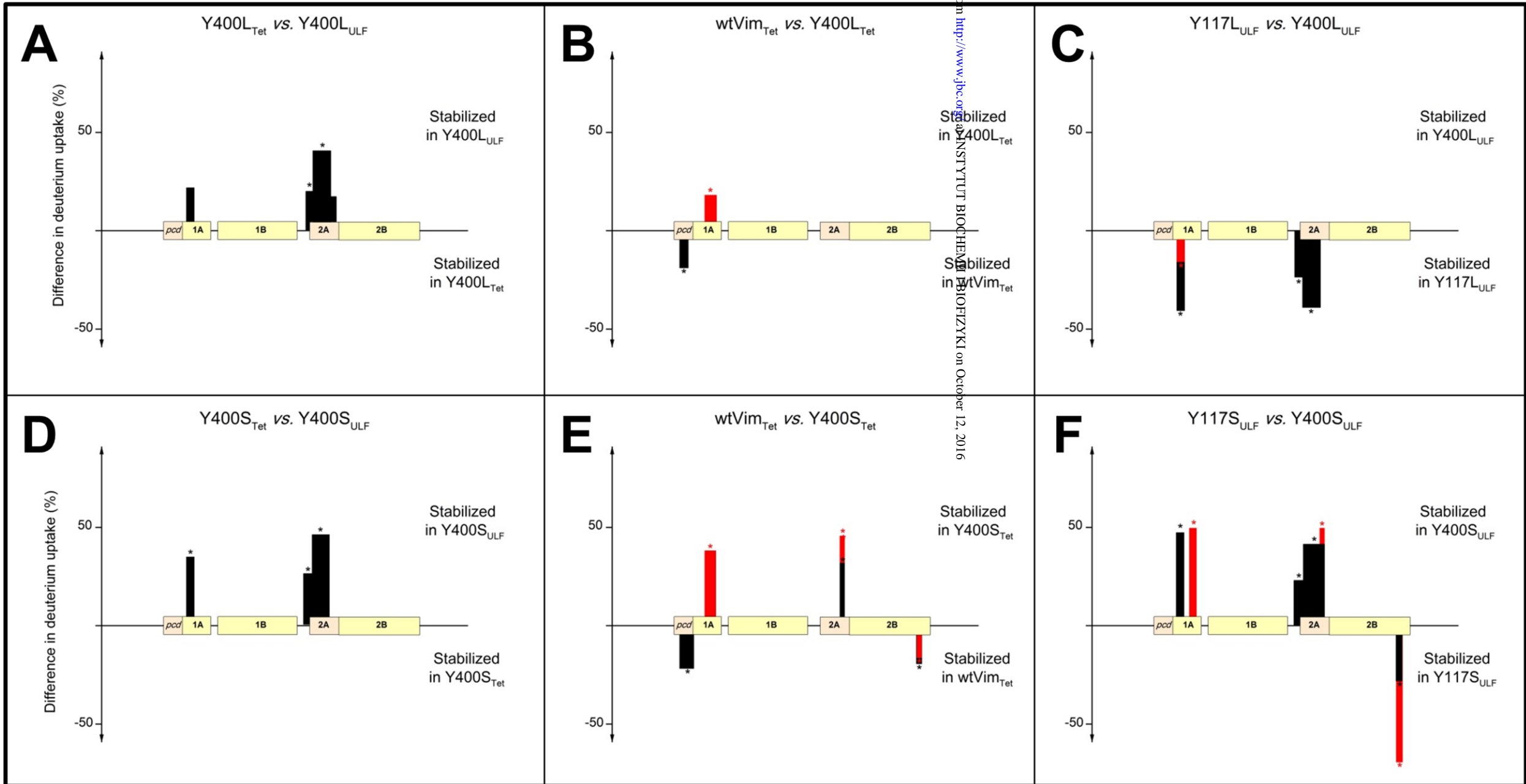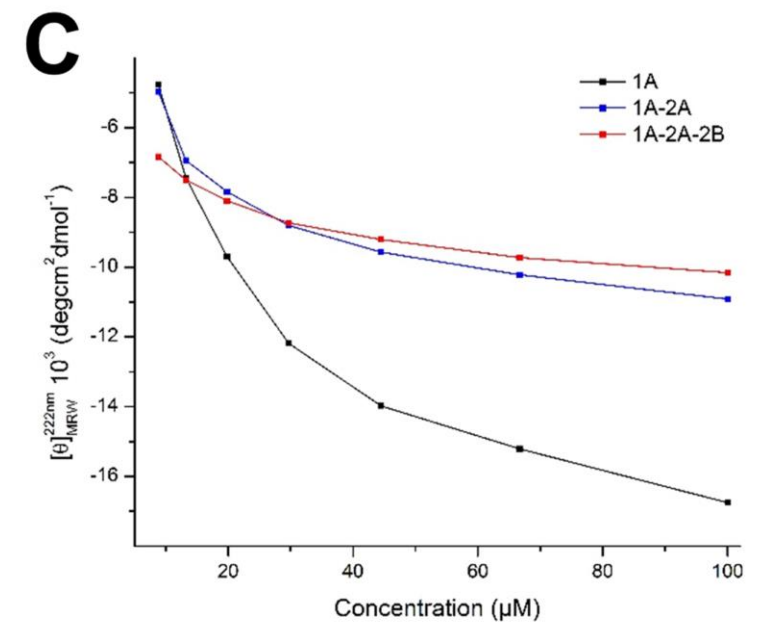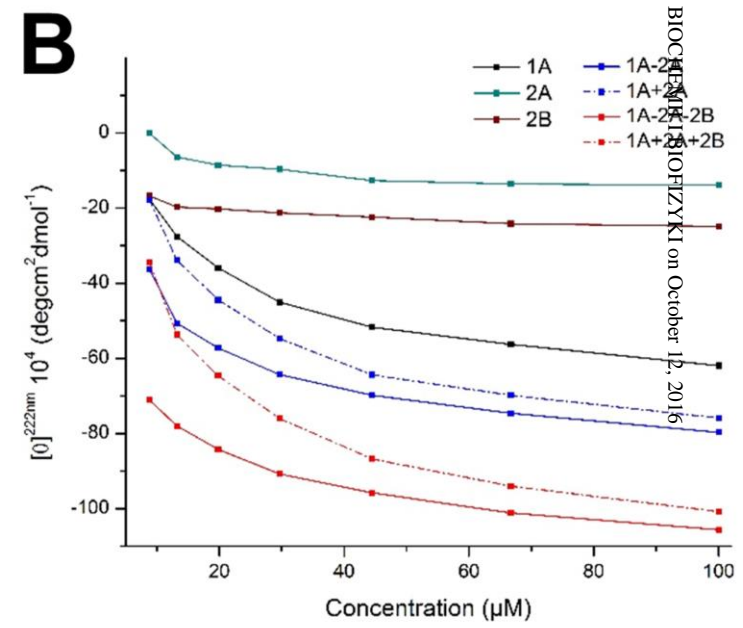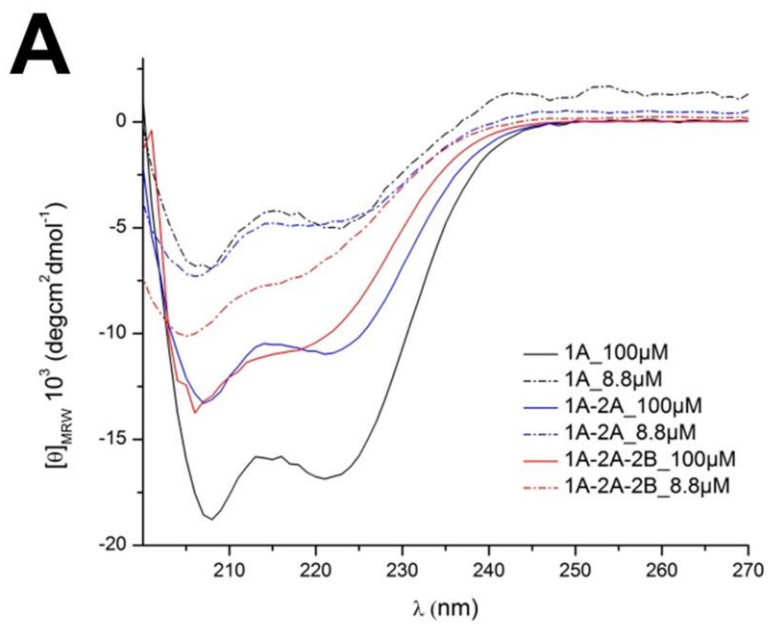
Figure 10

Table 1

Table 1. Amino acid sequences of linkers L1 and L12 in selected human intermediate filament proteins.

Protein name	SHC[a]	Positions L1[b]	Sequence[c]: linker L1 – coil 1B[d]	Position L12[b]	Sequence: linker L12
			139 0 1 2 3 4 5 6 7 - 8 9 0 1 2 3[e]		250 1 2 3 4 5 6 7 8 9 0 1 2 3 4[e]
Vimentin	III	139-147	KGQGKSRLG-DLYEEE	250-264	QEQHVQIDVDVSKPD
Desmin	III	144-152	KGREPTRVA-ELYEEE	255-269	QEQQVQVEMDMSKPD
GFAP	III	105-113	RAKEPTKLA-DVYQAE	216-230	ARQQVHVELDVAKPD
Peripherin	III	133-141	RGQEPARAD-QLCQQE	246-260	QQVQQVEVEATVKPE
α-internexin	IV	132-140	RHAEPSRVG-ELFQRE	246-260	SQAAAEVDVTVAKPD
NF-L	IV	128-136	KHSEPSRFR-ALYEQE	239-253	QYAQISVEMDVTKPD
NF-M	IV	139-147	KQASHAQLG-DAYDQE	251-265	ASHITVERKDYLKTD
NF-H	IV	135-143	QQAGRSAMG-ELYERE	252-266	QAQMQAETRDALKCD

[a] Sequence homology class

[b] First and last amino acids of the predicted linker region is given (see (13, 42)).

[c] One letter amino acid code

[d] The sequence of the N-terminal end of coil 1B begins after the dash

[e] Vimentin numbering of the amino acid sequence

Structural Dynamics of the Vimentin Coiled-Coil Contact Regions involved in Filament Assembly as revealed by Hydrogen-Deuterium Exchange

Aiswarya Premchandar, Norbert Mücke, Jaroslaw Poznanski, Tatjana Wedig, Magdalena Kaus-Drobek, Harald Herrmann and Michal Dadlez

Access the most updated version of this article at doi: 10.1074/jbc.M116.748145

Alerts:
- When this article is cited
- When a correction for this article is posted

Click here to choose from all of JBC's e-mail alerts

Supplemental material:
http://www.jbc.org/content/suppl/2016/09/30/M116.748145.DC1.html

This article cites 0 references, 0 of which can be accessed free at
http://www.jbc.org/content/early/2016/09/30/jbc.M116.748145.full.html#ref-list-1